THESIS FOR THE DEGREE OF LICENTIATE OF ENGINEERING

in

Thermo and Fluid Dynamics

Aerodynamic and Aeroacoustic Analysis of a Multi-Element Airfoil using Hybrid RANS/LES Modeling Approaches

by

Bastian Nebenführ

Department of Applied Mechanics
CHALMERS UNIVERSITY OF TECHNOLOGY
Göteborg, Sweden, 2012

Aerodynamic and Aeroacoustic Analysis of a Multi-Element Airfoil using Hybrid RANS/LES Modeling Approaches
Bastian Nebenführ

THESIS FOR LICENTIATE OF ENGINEERING no. 2012:14
ISSN 1652-8565

Department of Applied Mechanics
Chalmers University of Technology
SE-412 96 Göteborg
Sweden
Telephone +46-(0)31-7721000

This document was typeset using LaTeX

Printed at Chalmers Reproservice
Göteborg, Sweden, 2012

Aerodynamic and Aeroacoustic Analysis of a Multi-Element Airfoil

BASTIAN NEBENFÜHR

bastian.nebenfuhr@chalmers.se
Department of Applied Mechanics
Chalmers University of Technology

Abstract

Global hybrid RANS/LES simulations were used for computing the turbulent flow around a three-element airfoil. Based on the results of the flow computations, a comprehensive analysis of the flow properties was performed. The mean pressure distribution obtained from the simulations, was found to be in excellent agreement with experiments, when using an adequate spanwise domain extent and spanwise grid resolution. Initially, strong delays of the slat shear layer instability were observed, which could be overcome partly by adapting the grid resolution.

Moreover, unsteady flow data from the hybrid RANS/LES simulations was extracted at a permeable surface in the near-field of the airfoil and used as input for wave propagation calculations. Those calculations were done via three acoustic analogies, namely the Kirchhoff analogy, the Ffowcs-Williams and Hawkings analogy and the Curle analogy. In the present acoustical analysis, the performance of the three acoustic analogies is investigated. The noise contribution of all three elements of the airfoil was studied as well as their emission behavior.

Along with the aerodynamic and aeroacoustic analysis of the high-lift flow, hybrid RANS/LES modeling has been considered. As the so-called gray area problem of hybrid RANS/LES methods was encountered for the shear layer emanating from the slat cusp, several alleviation techniques were implemented and tested for a fundamental mixing layer flow.

Keywords: high-lift, multi-element airfoil, noise, CAA, hybrid RANS/LES, HYB0, Ffowcs-Williams and Hawkings, Kirchhoff, Curle

Acknowledgments

First of all, I would like to express my sincere gratitude towards my two supervisors, Lars Davidson and Shia-Hui Peng, who shared their knowledge and ideas with me. Thanks for your invaluable guidance and the fruitful discussions we had.

I would also like to thank Lars-Erik Eriksson, who introduced me to the world of aeroacoustics. In the same breath, the help and support by my colleague Huadong Yao is acknowledged, who deepened my knowledge about aeroacoustics and showed great patience in answering my countless questions.

Thanks to all my colleagues and friends at the department for creating a pleasant working atmosphere. Especially, my two office-mates, Guillaume and Pirooz: Thank you for making it a pleasure to come to work every morning.

I also have to thank my parents, without whom the adventure ”Sweden” would not have been possible for me.

Finally, I would like to thank Anke for loving, caring and encouraging. Ik ben een vrolijk kereltje, want ik heb jij!

The financial support of SNIC (the Swedish National Infrastructure for Computing) for computer time at C3SE (Chalmers Center for Computational Science and Engineering) is gratefully acknowledged. Furthermore, computer time at PDC (Center for High Performance Computing) at KTH Stockholm is acknowledged.

The work carried out during this thesis was financed by the EU project ATAAC (Advanced Turbulence Simulation for Aerodynamic Application Challenges), Grant Agreement No. 233710. Further information about the ATAAC project is provided at `http://cfd.mace.manchester.ac.uk/ATAAC/WebHome`.

List of publications

This thesis is based on the work contained in the following publications:

I B. Nebenfuhr, S.-H. Peng, and L. Davidson. Hybrid RANS-LES Simulation of Turbulent High-Lift Flow in Relation to Noise Generation. In S. Fu et al., editor, *Progress in Hybrid RANS-LES Modelling, NNFM*, volume 117. Springer, 2012.

II B. Nebenfuhr, H.-D. Yao, S.-H. Peng, and L. Davidson. Hybrid RANS-LES Simulation for Aerodynamic and Aeroacoustic Analysis of a Multi-Element Airfoil. To be published, 2013.

Nomenclature

Latin symbols

$\mathcal{N}(0,1)$	unit normal distribution
C	stowed chord length
c_0	speed of sound
C_P	pressure coefficient
C_s	slat chord length
k_{uvw}	turbulent kinetic energy (3D)
k_{uv}	turbulent kinetic energy (2D)
M	Mach number
N_x, N_y, N_z	components of unit normal vector
p	pressure
Re	Reynolds number
St	Strouhal number
T_{ij}	Lighthill tensor
U, V, W	streamwise, vertical and spanwise velocity
x, y, z	streamwise, vertical and spanwise coordinate
y^+	distance to wall in wall units

Greek symbols

α	incident angle
Δt	time step
Δx, Δy, Δz	streamwise, vertical and spanwise grid spacing
$\delta(f)$	Dirac delta
δ_{ij}	Kronecker delta
μ	dynamic viscosity
ν	kinematic viscosity
ψ	stochastic variable
ρ	density
τ	retarded time
τ_{ij}	stress tensor
θ	polar coordinate
$H(f)$	Heaviside function

Subscripts

∞	freestream quantity
C	Curle method
$corr$	corrected
exp	experimental
F	FWH method

K	Kirchhoff method
h	hybrid
t	turbulent quantity

Superscripts

$'$	fluctuating quantity
$\bar{\cdot}$	spatially filtered quantity or generalized derivative
$\vec{\cdot}$	vector

Symbols

∇^2	Laplace operator, $\nabla^2 = \frac{\partial^2}{\partial x_i \partial x_i}$
$\Box^2$	wave operator, $\Box^2 = \frac{1}{c_0^2}\frac{\partial^2}{\partial t^2} - \nabla^2 = 0$

Abbreviations

AoA	Angle of Attack
CAA	Computational AeroAcoustics
CFD	Computational Fluid Dynamics
CFL	Courant-Friedrichs-Lewy
DDES	Delayed Detached-Eddy Simulation
DES	Detached-Eddy Simulation
DNS	Direct Numerical Simulation
FWH	Ffowcs-Williams and Hawkings
GIS	Grid Induced Separation
HPF	High-Pass Filtering
HYB0	algebraic hybrid RANS/LES model
ICAO	International Civil Aviation Organization
IDDES	Improved Delayed Detached-Eddy Simulation
ILES	Implicit LES
LES	Large-Eddy Simulation
MSD	Modeled Stress Depletion
OASPL	OverAll Sound Pressure Level
PANS	Partially Averaged Navier-Stokes
PIV	Particle Image Velocimetry
RANS	Reynolds-Averaged Navier-Stokes
RMS	Root Mean Square
SA	Spalart-Allmaras
SA-DDES	DDES based on SA model
SA-DES	DES based on SA model
SGS	Sub-Grid Scale
SPL	Sound Pressure Level
URANS	Unsteady Reynolds-Averaged Navier-Stokes
WMLES	Wall-Modeled LES

Contents

Chapter 1

Introduction

In the last decades air traffic has constantly been increasing and is projected to further grow in the near future. At the same time, population densities in central Europe are relatively high and airports are often located in close proximity to residential areas. In order to protect the residents from the aircraft noise, regulations have been set-up by the International Civil Aviation Organization (ICAO). As of today, the radiated noise levels of all aircraft need to fulfill the requirements stated in Annex 16 of the Convention of International Civil Aviation [1], in order to be certified by the ICAO. Since the regulations become more and more stringent, the aircraft noise prediction and reduction have earned increased interest of the aircraft industry and airlines.

1.1 About aircraft noise

Only during the take-off and the approach and landing phases of a flight, the radiated noise of an aircraft is of practical importance. During these two instants of a flight, considerable noise levels can be perceived at the ground owing to the proximity of the aircraft. Especially during the approach of an airport, aircraft fly at low altitudes for large distances and hence affecting large areas with the radiated noise.

The two main sources of aircraft noise can be identified as the engines and the airframe. While at take-off the engines are working at full thrust and are dominating the noise signature of the aircraft, the engines are often at idle during approach and landing and hence their contribution gets less dominant. Additionally, due to the introduction of a new family of aero-engines, the so-called High-Bypass-Ratio engines, and the contemporary development of active and passive noise control devices, the engine noise contribution could be reduced significantly. Hence it can be shown as for instance in [2] that, during the approach phase, the airframe noise becomes a major contributor of aircraft noise. Because of that, research efforts have been focused on the prediction and reduction of airframe noise.

The airframe refers to all the structural parts of an aircraft, such as fuselage, wings, high-lift system, control surfaces and landing gear. Noise is created by the interaction of those structural parts with the high-speed airflow they are immersed in. It has been acknowledged that the high-lift system and the landing gear are the dominating sources of airframe noise. The high-lift system consists of move-

able elements, which can be deployed during take-off and landing in order to alter the shape of the airfoil. In that way, it is ensured that the aircraft can operate efficiently (that is without stall) at higher Angles of Attack (AoA) and at the low air speeds typical for the take-off and landing phases. Usual high-lift devices include a leading edge slat and one or several trailing edge flaps. The major part of the additional lift is created by the flap, while the slat directs the oncoming airflow in such a way that separation on the main wing is avoided. It is nowadays widely acknowledged that particularly the slat dominates the noise signature of an airfoil in high-lift configuration [3, 4, 5, 6].

1.2 Airframe noise prediction

An important step towards the development of efficient airframe noise reduction strategies is the accurate and reliable prediction of airframe noise.

1.2.1 Traditional aeroacoustics

Traditionally, the noise prediction was performed experimentally in wind tunnels on isolated wings [3, 7, 4, 8] or aircraft scale models [4, 8, 9]. Chow et al. [10] have even conducted some fly-over noise measurements on an Airbus A340. However, there are several drawbacks when using experimental prediction methods. Experiments require a rather detailed prototype and can be performed only at later stages in the development process of a new aircraft. If weaknesses in the acoustic design are discovered in the measurements, changes have to be made in an ad-hoc manner or are costly due to re-design and delays in the launch of the new product. Moreover, wind tunnels for entire aircraft need to be large and are expensive to run, which leads to the testing of scale models. Even though scaling laws for the radiated noise are developed, uncertainties in terms of the scale effects remain.

1.2.2 Computational aeroacoustics

Numerical predictions of airframe noise can be performed with the help of Computational Fluid Dynamics (CFD) simulations. This new approach is referred to as Computational AeroAcoustics (CAA). For a CAA approach to be of industrial relevance, results have to be provided in a rapid and accurate manner. Over-night results would be desirable, but seem out of reach for now. However, due to the steady increase of computational power, the CAA approach has become feasible nowadays.

In the beginning, two-dimensional Unsteady Reynolds-Averaged Navier-Stokes (URANS) simulations were used by Khorrami et al. [11] for the investigation of near-field slat noise sources. Using this input data, Singer and co-workers [12] predicted the far-field noise signature of a three-element airfoil with the help of the Ffowcs-Williams and Hawkings (FWH) acoustic analogy [13]. Three-dimensional unsteady simulations have been carried out using URANS with a switched-off production term in the region of interest [14, 15]. Also hybrid RANS/LES approaches are considered to be a promising candidate for the prediction of high-lift noise. Their feasibility for predicting the aerodynamics of high-lift flows has been shown by Deck [16, 17].

Recently, hybrid RANS/LES approaches in combination with acoustic analogies have also been employed for noise prediction [18, 19, 20, 21].

Since virtual models are investigated in CAA, no real prototype of the wing needs to exist. As a consequence, the aeroacoustic assessment can be carried out at a much earlier stage of the development process and the the pitfalls described for the experimental approach can be circumvented. An overview over the CAA methods available in 2004 and a future outlook of the development of CAA tools was given by Singer and Guo [22].

1.3 Scope of this work

In the present work, focus is placed on the numerical investigation of airframe noise due to the high-lift devices of a multi-element airfoil. In order to carry out a comprehensive analysis of the aerodynamic and aeroacoustic properties of the high-lift airfoil, global hybrid RANS/LES modeling approaches are used. For the prediction of far-field noise, based on the unsteady data provided by the hybrid RANS/LES computation, three acoustic analogies, namely the Kirchhoff surface integral method [23], the Ffowcs-Williams and Hawkings method [13, 24] for a stationary, permeable surface and the Curle method [25] are employed.

Generally, hybrid RANS/LES approaches are considered a good candidate for providing the unsteady information needed in acoustical analogies. However, conventional hybrid RANS/LES methods still suffer from various shortcomings, of which two, namely Modeled Stress Depletion and the gray area problem are high-lighted in this work as well. Substantial effort was invested in tackling the latter shortcoming.

This thesis is structured as follows. Firstly, an overview over the field of hybrid RANS/LES simulations including a brief description of the hybrid RANS/LES modeling approaches employed in this work is given in Section 2. In the same section, also the treatment of two of the major shortcomings of hybrid RANS/LES methods is illustrated. Section 3 is devoted to the description of the three acoustic analogies. In Section 4, the geometry of the high-lift airfoil along with the numerical procedure is explained. A summary of the main findings is given in Section 5. Finally, in Section 6, this work is concluded and recommendations for future research efforts are given.

Chapter 2

Hybrid RANS/LES

2.1 State of the Art in Hybrid RANS/LES modeling

As of today, RANS simulations are widely used in industrial CFD. Numerous well adjusted RANS turbulence models exist, which have been evaluated for a large variety of flows. In that sense, RANS has proved to be a valid tool for many aerodynamic problems of industrial importance. More recently, new challenges, such as the prediction and control of aerodynamic noise and the investigation of unsteady aerodynamic loads, require unsteady information about the flow that conventional steady RANS methods fail to provide. In Direct Numerical Simulation (DNS), all turbulent length- and time-scales are resolved, which is considered to give the most accurate results. At the same time, DNS is out of question for industrial applications, due to excessive computational demands. DNS is hence limited to fundamental test cases at low Reynolds number. RANS methods model all turbulent scales, which is a task of particular difficulty for the largest scales in a turbulence spectrum, since they usually are geometry dependent. As the largest scales carry most of the energy, their accurate representation is inevitable for a trustworthy result. In Large-Eddy Simulations (LES) the large turbulent scales are resolved, while only the smallest scales, i.e. the ones smaller than the grid spacing, are modeled with a so-called Sub-Grid Scale (SGS) model. Often simple SGS models are found to be sufficient as the small scale turbulence is assumed to be of isotropic nature and thus easy to model. Also, LES on fairly coarse grids may suffice for capturing the physics of flows dominated by large scale turbulence. However, the presence of solid walls in a computational domain proves to be problematic for LES. When solid boundaries are approached, even the large turbulent scales are becoming small and in order to accurately represent the turbulence in a boundary layer, excessively fine near-wall grids have to be used. Due to the grid requirements, Spalart [26] suggest to consider LES with a well-resolved near-wall region as quasi-DNS. Except for jets and flames, most industrial flows involve solid walls, which rules out LES as a candidate. Even though computational power is increasing dramatically nowadays, LES is predicted to be out of reach for high-Reynolds number flows for the next decades [27, 26]. In fact, Spalart et al. [27] estimate LES of a full wing to not be possible before the year 2045.

As a consequence, hybrid methods that combine the strengths of RANS and LES, namely a relaxed grid requirement for the wall-parallel plane in the near-wall region

and the capability of accurately capturing the flow physics away from solid walls, were developed. Those methods are in the following referred to as hybrid RANS/ LES methods. Principally, four different kinds of hybrid RANS/LES approaches can be distinguished:

1. Global approaches
2. Zonal approaches
3. Seamless methods
4. Wall-Modeled LES (WMLES)

2.1.1 Global approaches

Conventional RANS is well calibrated and tested for attached boundary layer flows and is able to compute those reasonably well. As noted above, LES has its strengths in computing detached flows with large scale turbulence as it is the case after flow separation. Global approaches seek to combine RANS and LES in one single universal method. More specifically, the attached near-wall region is treated in URANS mode, whereas the flow away from the wall is treated in LES mode, as schematically shown in Fig. 2.1. For this purpose, the SGS model usually is taken as a counterpart of the underlying RANS model. The RANS requirements for the grid resolution in the wall-parallel directions are much more relaxed than for LES, which results in a considerable reduction of the grid cells required and hence makes it feasible to compute flows at engineering Reynolds numbers. Note, however, that even for RANS the wall-normal grid spacing has to be comparable to that of LES. This means that the only advantage in terms of grid resolution is associated to the wall-parallel plane. Probably the most prominent global approach is the Detached-Eddy Simulation (DES) proposed by Spalart et al. in 1997 [27]. The idea of DES is to use a RANS model to treat the boundary layer flow and to switch to LES, once the flow has separated. Based on a comparison between the local grid spacing and the wall distance, DES decides automatically, whether the RANS or LES branch has to be activated. In order to ensure the desired behavior, care has to be taken during the generation of DES grids. That is, the grid spacing in the wall-parallel plane has to exceed the local boundary layer thickness, δ. Originally, DES was invented for the use in massively separated flows, such as an airfoil in deep stall. In such a case, the attached boundary layers are thin and the separated region is dominated by large scale turbulence. A schematic drawing of such a case is provided in Fig. 2.2.

It has been anticipated by the authors [27] that in case of thick boundary layers or uncareful grid generation, the wall-parallel grid spacing can become smaller than the boundary layer thickness and a phenomenon called Modeled Stress Depletion (MSD) can occur. If the LES mode is activated inside the boundary layer, the length scale is reduced, which in turns leads to a decrease in eddy viscosity. Consequently, the modeled stresses are reduced, even though the grid is not fine enough to support resolved stresses. Due to the subsequent reduction of skin friction caused by MSD, premature separation can occur in severe cases, as shown by Menter and Kuntz in

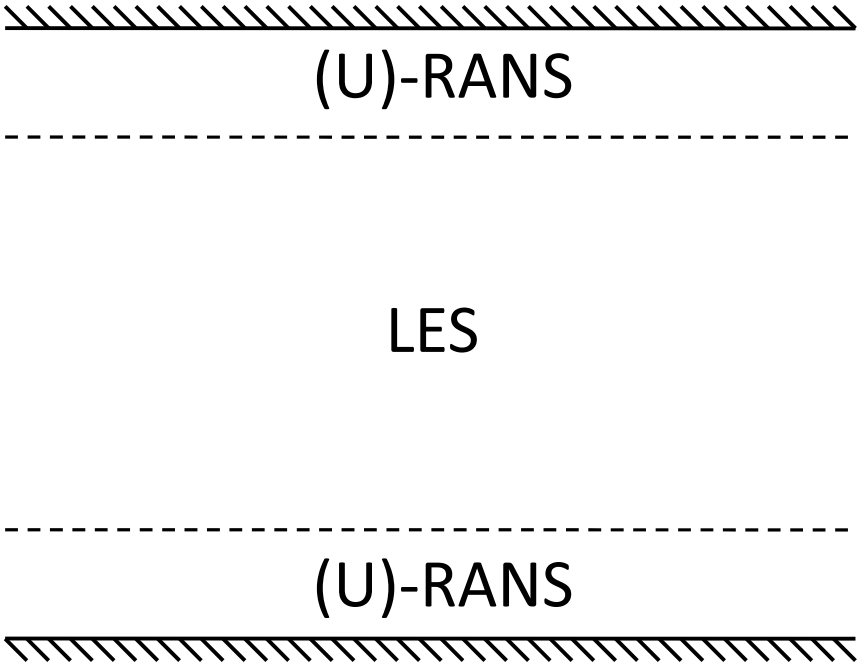

Figure 2.1: Schematic drawing of a typical hybrid RANS/LES method for a channel flow. (U)-RANS in the boundary layer, LES outside the boundary layer.

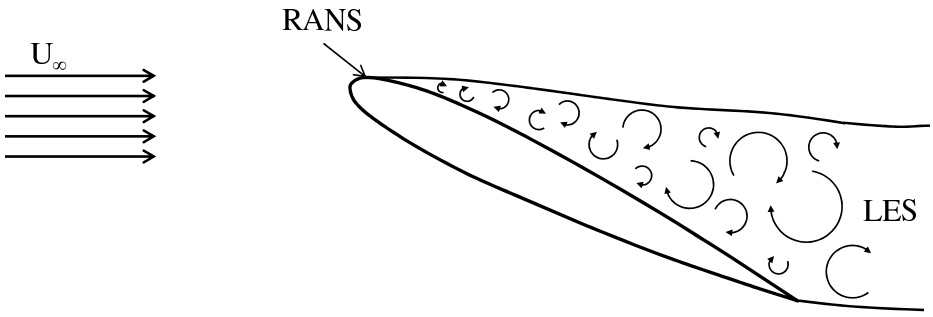

Figure 2.2: Schematic drawing of a natural DES application.

[28, 29]. This phenomenon of premature separation is termed Grid Induced Separation (GIS). Initial solutions to MSD and GIS have been proposed by Menter and Kuntz [28], who suggest using a shielding function for the boundary layer, and by Deck [30], who proposes to make the DES approach zonal, i.e. disable the DES limiter in critical regions. In 2006, a nowadays commonly used remedy, termed Delayed DES (DDES), was presented by Spalart et al. [31]. Based on the idea of Menter and Kuntz [28], RANS mode is preserved in the boundary layer with a shielding function.

All global hybrid RANS/LES methods suffer from a certain ”gray area” at the interface between RANS and LES, as described by Spalart [32]. In this gray area, the computation cannot really be considered RANS, as the eddy viscosity and, subsequently, also the modeled stresses are gradually decreased. At the same time, no (or very little) resolved fluctuations are present, as they either have to come from the RANS region or have to gradually build up. The gray area can hence lead to

substantial delays in the formation of instabilities and three-dimensional turbulence content. Moreover, high values of eddy viscosity usually are convected from the RANS into the LES region, which amplifies the delay in the formation of LES content. Cases with a geometrically defined separation location usually suffer less from the gray area issue than cases with shallow separation. Illustrative examples of both MSD, GIS and the gray area issue are given in Section 2.4.

2.1.2 Zonal approaches

In zonal methods designated zones that are treated by RANS or LES are specified. The RANS and LES zones can be principally defined in two ways. Firstly, the near-wall region can be specified as a RANS region, which leads to a situation similar to the one shown in Fig. 2.1. The interface between RANS and LES is then prescribed at a constant grid line parallel to the wall as exercised by Davidson and Peng [33] and Davidson and Dahlstrm [34]. Based on the idea that most of the flow in a large domain can be treated as (quasi-) steady RANS, it is also possible to only specify LES in a small region of interest. In that case, the LES zone is surrounded by RANS regions and these kind of approaches are also referred to as Embedded LES.

While in global methods the RANS turbulence model is manipulated in order to be able to function as an equivalent SGS model in the LES region, the models used in the RANS and LES zones do not necessarily resemble each other in zonal methods. Note that the acronym ”LES” is used representative of virtually any turbulence resolving method, such as, for instance, well-resolved LES, WMLES, DES or DDES. An example of a generic zonal approach is given in Fig. 2.3 for the case of separation on an airfoil. Note that, in principle, the problem of MSD and GIS can be avoided completely using zonal methods by carefully defining the RANS and LES zones. As the respective RANS and LES zones have to be specified at the grid generation stage, a considerable amount of knowledge about the expected flow topology has to be available a-priori. The decision load on the user is hence usually greater than for global methods.

Even though the safety from MSD and GIS is theoretically provided in zonal methods, the gray area issue described for global methods, also can occur in zonal approaches. Unlike in global methods, the interface location of RANS and LES is known. An obvious solution to the gray area issue in zonal methods is then to introduce LES content at the RANS/LES interface. This procedure is known as forcing and is similar to providing unsteady inlet conditions for LES or DNS. The injected turbulent content can, for example, stem from either synthetic turbulence, as described by Davidson and Billson [35], or from a precursor DNS as in [34]. In some cases [36, 37] also ”recycled” fluctuations from a downstream location have been successfully injected. As the impact of injecting synthetic fluctuations at the RANS/LES interface is unknown, some authors recommend to avoid this procedure [38]. However, the treatment of injected turbulent content is beyond the scope of the present work. Furthermore, it should be mentioned that such a treatment is not applicable to global methods, as the interface location is not known a-priori and might even be time-dependent.

Besides the higher decision load on the user, zonal approaches prove to be surprisingly versatile. For instance, a complex flow can be broken down (through spec-

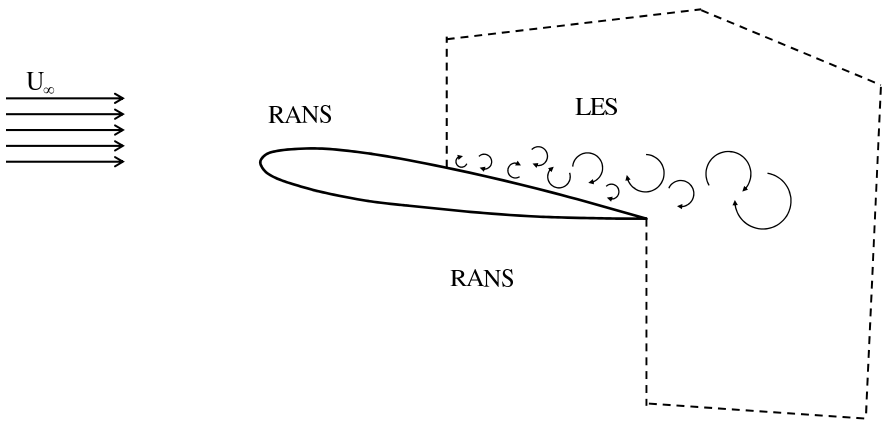

Figure 2.3: Schematic drawing of a zonal LES approach. The dashed line represents the RANS/LES interface.

ification of zones) into multiple generic flow problems, for each of which the most appropriate turbulence resolving method can be specified.

Also two different strategies of using zonal approaches can be identified. Firstly, it is possible to run RANS and LES during one simulation, as it would be the case in global methods. This allows for some coupling between the RANS and LES zones. More specifically, the RANS zones can receive feedback from the LES zones. Typical examples of such strategies are the Zonal DES (ZDES) approach by Deck [30, 17] and the aforementioned zonal hybrid RANS/LES approaches of Davidson and Peng [33] and Davidson and Dahlstrm [34]. Secondly, computations of RANS and LES can be carried out separately. Initially, the RANS computation is carried out in the entire domain, which provides the boundary conditions for the turbulence resolving simulations in the LES zones. In that case, it can even be sufficient, to run two-dimensional RANS. When the RANS and LES computations are carried out in a decoupled manner, there is no possibility of feedback from the LES to the RANS region. An example of such a strategy is the Non-Linear Disturbance Equations approach [39, 40] as used for instance by Terracol [41].

2.1.3 Seamless methods

Unlike in global or zonal approaches, in seamless methods there is no sharp interface between RANS and LES. Partial-Averaged Navier-Stokes (PANS) [42, 43] is considered to be a typical example of a seamless approach. In PANS the ratio of resolved to unresolved turbulent quantities is specified by the user, which leads to a homogeneous mixture of RANS and LES in the domain. If a k-equation PANS method is considered, then a constant f_k defines the ratio of unresolved to total kinetic energy. Setting $f_k = 1$ returns pure RANS and $f_k = 0$ would return DNS. Davidson [44] has used a $k - \varepsilon$ PANS in a zonal manner by specifying different values of f_k in order

to obtain RANS and LES zones. This is a strong deviation from the original PANS idea, as the coefficient f_k was initially not considered to be a constant.

2.1.4 Wall-Modeled LES

Another idea in hybrid RANS/LES modeling has been to use wall-modeling in LES (WMLES). In comparison to DES or DDES, in WMLES the switch from RANS to LES is performed much closer to the wall, i.e. inside the boundary layer, which means that a greater portion of the turbulence is resolved. In that sense, the RANS model works as a wall function. One strategy for WMLES, termed Improved DDES (IDDES), has been proposed in 2008 by Shur et al. [45]. The basic idea of IDDES is for the model to act as WMLES, if the inflow conditions and the grid support such behavior. The inflow conditions must contain turbulent content and the grid is required to be fine enough to resolve boundary layer eddies. In case those prerequisites are not fulfilled, IDDES will perform as conventional DDES.

2.2 Common hybrid RANS/LES approaches

Some of the most common hybrid RANS/LES modeling approaches are described briefly below. All of the described models have been employed during this work.

2.2.1 DES based on the SA model (SA-DES)

DES can be implemented for any underlying RANS model, but here the original version, as proposed by Spalart [27] is presented. In the original version, DES was derived for the the Spalart-Allmaras (SA) one-equation RANS model [46]. A single transport equation for a viscosity-like quantity, $\tilde{\nu}$ is solved in the SA model.

$$\frac{D\tilde{\nu}}{Dt} = c_{b1}\tilde{S}\tilde{\nu} + \frac{1}{\sigma}\left[\nabla\cdot((\nu+\tilde{\nu})\nabla\tilde{\nu}) + c_{b2}(\nabla\tilde{\nu})^2\right] - c_{w1}f_w\left[\frac{\tilde{\nu}}{d_w}\right]^2 \tag{2.1}$$

where c_{b1}, c_{b2}, c_{w1} and σ are model constants, d_w is the distance to the nearest wall and f_w is a wall-damping function. In the production term, $\tilde{S}$ is the vorticity magnitude modified by another damping function f_{v2}, such that correct log-layer behavior is retained, i.e. $\tilde{S} = u_\tau/\kappa y$ with u_τ being the friction velocity. Yet another damping function, f_{v1}, is used to obtain the eddy viscosity as $\nu_t = \tilde{\nu}f_{v1}$, which now also behaves correctly in the log-layer. When balancing the production and destruction terms in Eq. (2.1) one can show that $\nu_t \propto Sd_w^2$. In the Smagorinsky SGS model [47], the SGS eddy viscosity is formulated with the strain rate tensor magnitude, S[a], and the grid spacing, Δ, as $\nu_{SGS} \propto S\Delta^2$. Replacing d_w in the SA model by a modified length scale based on the grid spacing, Δ, will make the model act as a SGS model. This behavior can be implemented as in Eq. (2.2),

$$\tilde{d} = \min(d_w, C_{DES}\Delta) \tag{2.2}$$

[a] Note the ambiguity in the use of S. In the SA model, S is the vorticity magnitude and in the Smagorinsky SGS model, $S = \sqrt{2S_{ij}S_{ij}}$

where C_{DES} is the DES constant. Now, the model will act as a RANS model, when $d_w < \Delta$ and as a SGS model, when $d_w > \Delta$. The switch between RANS and LES is thus dependent on the local grid density. In DES, Δ is taken as the maximum grid spacing, i.e. $\Delta = \Delta_{max} = \max(\Delta x, \Delta y, \Delta z)$. The RANS requirement on the grid spacing in the boundary layer leads to anisotropic grids near the wall, where $\Delta x \approx \Delta z \gg \Delta y$. Subsequently d_w is likely to be smaller than Δ here and hence RANS behavior is obtained as desired. Outside the boundary layer, the grid spacing is likely to be more isotropic and $\Delta < d_w$, which modifies the length scale and hence makes the model perform as a SGS model. Recall, that the basic idea of DES was to treat the entire boundary layer in RANS mode. Hence the requirement for correct behavior is that the grid spacing in the wall-parallel plane exceeds the local boundary layer thickness, δ. As mentioned earlier, ambiguous grids with a wall-parallel spacing Δ_{max} smaller than δ lead to the problems of MSD and GIS. Many practical situations occur in which the grid spacing becomes ambiguous, such as for example grid refinement towards the trailing edge of an airfoil. In those cases, MSD and GIS cannot be avoided with conventional DES.

2.2.2 Delayed DES based on the SA model (SA-DDES)

The idea of DDES is to protect the boundary layer from intrusion by the LES mode and hence to guarantee correct RANS behavior. Inspired by the proposal of Menter and Kuntz [28], a shielding function was developed by Spalart and co-workers [31]. At the example of DDES based on the SA model, the shielding function reads:

$$f_d = 1 - \tanh([8r_d]^3) \tag{2.3}$$

The function is designed to be equal 1 in the LES region and 0 elsewhere. This is achieved with the parameter r_d, which is designed to equal 1 in a logarithmic layer and to gradually decrease to 0 at the outer boundary layer edge. The parameter r_d is defined as follows:

$$r_d = \frac{\nu_t + \nu}{\sqrt{U_{i,j}U_{i,j}}\kappa^2 d_w^2} \tag{2.4}$$

In Eq. (2.4), ν_t and ν are the eddy viscosity and the molecular viscosity, respectively, the expression $U_{i,j}$ denotes the velocity gradients [b], κ is the von Kármán constant and d_w is the wall distance. Based on the shielding function of Eq. (2.3), the DES length scale is redefined in DDES.

$$\tilde{d} = d_w - f_d \max(0, d_w - C_{DES}\Delta) \tag{2.5}$$

One can see now, that $f_d = 0$ returns RANS behavior, while $f_d = 1$ yields the length scale used in the original DES as given in Eq. (2.2). Note, that DDES does prevent MSD for a large number of cases, but at the same time the gray area issue for free shear layers is amplified by its use.

[b] The expression $U_{i,j}$ is equivalent to $\frac{\partial U_i}{\partial x_j}$.

2.2.3 An algebraic hybrid RANS/LES model (HYB0)

Recently, Peng has developed an algebraic hybrid RANS/LES model [48, 49], which combines a mixing-length RANS model in the near-wall region with the Smagorinsky SGS model [47] in the off-wall LES region. As no additional transport equation has to be solved in this model, we also refer to it as a zero-equation hybrid RANS/LES model or the HYB0 model. Simple algebraic RANS models have shown to be robust and efficient in modeling attached boundary layers, as, for example, by Baldwin and Lomax [50]. Due to the simplicity of the model, shorter computation times are achieved by the HYB0 model as compared to DES based on one- or two-equation RANS models.

In the near-wall RANS mode, the eddy viscosity is formulated according to the mixing-length concept as in Eq. (2.6)

$$\tilde{\mu}_t = \rho \tilde{l_\mu}^2 S \tag{2.6}$$

where $\tilde{l}_\mu$ is the turbulent length scale and $S = \sqrt{2S_{ij}S_{ij}}$. The strain rate tensor is defined as $S_{ij} = 0.5(\partial u_i/\partial x_j + \partial u_j/\partial x_i)$. The turbulent length scale is proportional to the wall distance, d_w, and is defined by

$$\tilde{l}_\mu = f_\mu \kappa d_w \tag{2.7}$$

where $\kappa = 0.418$ is the von Kármán constant. In the above equation, f_μ represents an empirical damping function, based on the viscosity ratio in the RANS region $R_t = \tilde{\mu}_t/\mu$. The damping function reads

$$f_\mu = \tanh\left(\frac{R_t^{1/3}}{2.5}\right) \tag{2.8}$$

Away from the wall, in the LES region, the Smagorinsky SGS model is employed with the SGS eddy viscosity as follows:

$$\mu_{SGS} = \rho(C_s\Delta)^2 S \tag{2.9}$$

with $C_s = 0.12$ and

$$\Delta = \sqrt{\frac{(\Delta_{max}^2 + \delta V^{2/3})}{2}} \tag{2.10}$$

where δV denotes the local control volume of one node and Δ_{max} is the maximum edge length of the control volume, i.e. $\Delta_{max} = \max(\Delta x, \Delta y, \Delta z)$. A crucial step in developing efficient hybrid RANS/LES models is the design of the matching between the two modes. Here, the RANS length scale, $\tilde{l}_\mu$, is modified over the RANS/LES interface by multiplying with an empirical matching function, i.e. $l_\mu = \tilde{l}_\mu f_s$. This results in the following eddy viscosity in the RANS region:

$$\mu_t = \rho l_\mu^2 S \tag{2.11}$$

The matching function, f_s, reads

$$f_s = \frac{1}{2}\left[\exp\left(-\frac{R_s^{0.75}}{4.75}\right) + \exp\left(-\frac{R_s^{0.3}}{2.5}\right)\right] \tag{2.12}$$

where $R_s = \tilde{\mu}_t/\mu_{SGS}$ is the ratio of the eddy viscosities in the RANS and LES regions. Finally, the hybrid eddy viscosity, μ_h, is chosen according to:

$$\mu_h = \begin{cases} \mu_t, & \text{if } \tilde{l}_\mu < \Delta, \\ \mu_{SGS}, & \text{if } \tilde{l}_\mu \geq \Delta. \end{cases} \tag{2.13}$$

2.3 Dealing with the gray area problem

The gray area problem in hybrid RANS/LES methods can lead to delayed instabilities of free shear layers, which are non-physical. Kok and van der Ven [51] have identified four possible causes for this behavior.

1. Turbulence model does not switch to LES mode
2. Shear layer instabilities are not triggered as no turbulent content is available
3. Eddy viscosity and SGS stresses are too high
4. Numerical errors are too high

The first cause can easily be treated by using a zonal approach, as suggested by Deck [30, 17] or Davidson and Peng [52], as the zones with solely RANS or LES behavior are explicitly defined. In terms of global methods, an easy solution is not available, but solutions to cause 2 and 3 might redeem also cause 1.

Often second-order accurate schemes are used in hybrid RANS/LES. Kravchenko and Moin [53] demonstrate that numerical errors can be of the same order as the SGS stresses and that high-order schemes can significantly improve the results. Due to that, high-order accuracy schemes have been developed lately, as for instance by Kok [54]. In the present work, focus was put on the 2nd and 3rd cause mainly and a couple of approaches that help mitigate the gray area problem are described below.

2.3.1 Energy backscatter

In turbulent flows, it is commonly assumed that large eddies extract kinetic energy from the mean flow, which they then transfer to subsequently smaller eddies. This process is often referred to as the energy cascade. In the smallest eddies of the spectrum, viscous effects help to dissipate the kinetic energy into heat. Even though this is true in average, locally reverse energy transfer (from small to large eddies) can occur [55, 56]. The reverse energy transfer is often referred to as energy backscatter and is not accounted for in usual eddy viscosity turbulence models, which are strictly dissipative.

Peng [57] suggests that the energy backscatter can be used for triggering the unstable modes of a shear layer and thus help to more quickly generate turbulent content. One can reconstruct all the terms of the SGS stress tensor with the help of a Taylor expansion.

$$\begin{aligned} \tau_{ij} &= (\overline{u_i u_j} - \bar{u}_i \bar{u}_j) \\ &= \bar{\Delta}^2 \frac{\partial \bar{u}_i}{\partial x_k} \frac{\partial \bar{u}_j}{\partial x_k} + \frac{\bar{\Delta}^4}{2!} \frac{\partial^2 \bar{u}_i}{\partial x_k \partial x_l} \frac{\partial^2 \bar{u}_j}{\partial x_k \partial x_l} + \cdots \end{aligned} \tag{2.14}$$

The first term of the Taylor series is capable of providing energy backscatter, but is not sufficiently dissipative in itself. For that reason, Peng and Davidson [58] and Peng [57] combine the backscatter term with a conventional eddy viscosity term, which yields a mixed model.

$$\tau_{ij} = \tau_{L,ij} + \tau_{S,ij} = (C_L\Delta)^2 \frac{\partial u_i}{\partial x_k}\frac{\partial u_j}{\partial x_k} - 2\nu_{SGS}S_{ij} \tag{2.15}$$

In Eq. (2.15), $\tau_{L,ij}$ is called the Leonard term representing the term capable of energy backscatter, $\tau_{S,ij}$ is the conventional eddy viscosity term providing sufficient dissipation and C_L is a model constant that has to be calibrated. Note, that in Eq. (2.15), the overbar denoting spatial filtering has been dropped. The suggested modification can be applied to any eddy viscosity turbulence model.

A similar application of backscatter has been suggested by Davidson [59]. Backscatter of a scale-similarity model is used as forcing at the interface of a hybrid RANS/ LES method. In order to provide the desired effect, only the instances of the additional stresses that lead to backscatter are considered. All instances of the stresses that lead to additional energy dissipation, are neglected.

2.3.2 Stochastic SGS model

A similar idea is presented by Kok and van der Ven [60], who believe that the randomness in the turbulence spectrum can be stimulated by stochastic forcing. A random walk process is used in order to provide a stochastic variable, ψ, which is multiplied with the eddy viscosity in the LES region.

$$\nu_{SGS} = \psi^2\tilde{\nu}_{SGS} \tag{2.16}$$

A new value for the stochastic variable is drawn at each time step and for each grid point from a unit normal distribution, so that $\psi = \mathcal{N}(0,1)$. Also this modification is easily implemented for any type of eddy viscosity turbulence model.

2.3.3 High-Pass Filtering (HPF)

While the first two modifications dealt with cause 2, the following suggestions are focused on tackling cause 3. Too high SGS stresses may hamper or even suppress the development of the small instabilities in a shear layer. One way to circumvent high stresses is to switch off the SGS model entirely, which helps to speed-up shear layer instabilities considerably. LES methods without SGS model rely on the dissipation provided by the numerical method and are called Implicit LES (ILES). Such a treatment was exercised by Shur et al. [38] for jet flows.

The Boussinesq assumption bases the stresses and the eddy viscosity on the mean velocity gradients. In the thin, initial state of a free shear layer, the mean velocity gradient is high, leading to high modeled stresses. There is little evidence that the stresses should actually be based on the mean velocity gradient. An effort to reduce the stresses is hence, to base the stresses on the gradients of the velocity fluctuations.

$$\tau_{ij} = \nu_{SGS}\left(\frac{\partial u_i'}{\partial x_j} + \frac{\partial u_j'}{\partial x_i}\right) - \frac{2}{3}k\delta_{ij} \tag{2.17}$$

Kok and van der Ven proposed to perform high-pass filtering based on a running time-average [51]. Earlier proposals involved spatial filtering [61]. Besides the stresses itself, in a Smagorinsky-type SGS model also the eddy viscosity can be computed based on the gradient of the fluctuations.

$$\nu_{SGS} = (C_{SGS}\Delta)^2(S') \tag{2.18}$$

where $S' = \sqrt{2S'_{ij}S'_{ij}}$, with the strain rate due to the velocity fluctuations, $S'_{ij} = 0.5(\partial u'_i/\partial x_j + \partial u'_j/\partial x_i)$. Note that, due to the need of averaging and storage of an additional quantity, the computational effort increases. Nevertheless, the implementation is straight forward for any type of eddy viscosity SGS model.

2.3.4 Alternative length scale

Typically the maximum edge length of the grid cell is used as the filter width, $\Delta = \Delta_{max} = \max(\Delta x, \Delta y, \Delta z)$ in DES-type methods. In case of a plane free shear layer, the grid might be designed in a way so that highly anisotropic cells can be found in the shear layer with the largest dimension in the spanwise direction. Even though the grid might be quite well resolved in the $x - y$ plane, the spanwise constraint on the cell size will lead to high values of eddy viscosity, which delays the development of instabilities. Breuer et al. [62] advocate the use of the cubic root of the control volume as the filter width (as in LES), i.e. $\Delta = \Delta_{vol} = (\Delta x \Delta y \Delta z)^{1/3}$, which leads to dramatically improved shear layer predictions. However, Spalart [32] criticizes the lack of physical justification for using such a filter width.

Chauvet et al. [63] suggest an alternative approach, based on the local vorticity. Arguing that only the resolution of the grid plane perpendicular to the local vorticity vector is used for resolving the rotational motion of the flow, the following expression of the filter width is derived.

$$\Delta = \sqrt{N_x^2\Delta y\Delta z + N_y^2\Delta x\Delta z + N_z^2\Delta x\Delta y} \tag{2.19}$$

In the above equation, the N_i are the components of the unit normal vector $\vec{N} = \vec{\omega}/|\vec{\omega}|$ that indicates the orientation of the vorticity. The effect of using this filter width has been demonstrated by Deck [17]. However, the use of this filter width is only straight forward in cases of a structured grid and when the vorticity vector is aligned with one of the principle grid dimensions. Even though, the implementation of the alternate length scale is possible for any hybrid RANS/LES method, its use does increase the models tendency to MSD, since the switch between RANS and LES is shifted inside the boundary layer.

2.4 Illustrations of shortcomings

The aforementioned shortcomings of hybrid RANS/LES methods, namely MSD, GIS and the gray area problem were encountered for the high-lift flow. However, they can be illustrated on the more fundamental cases of a backward facing step flow and a flat plate mixing layer flow, respectively.

2.4.1 MSD and GIS

A prime example of MSD with subsequent GIS can be presented for the top wall of a back-step flow using SA-DES. Due to the use of a structured grid and the desire to keep a wall normal grid spacing of $y^+ \approx 1$ at the step wall, LES behavior is triggered inside the boundary layer at the top wall, right above the step. This leads to a significant reduction of the eddy viscosity and hence the modeled stresses (Fig. 2.4(a)). The stresses are depleted so deeply that the flow separates from the top wall, as illustrated by Fig. 2.5(a).

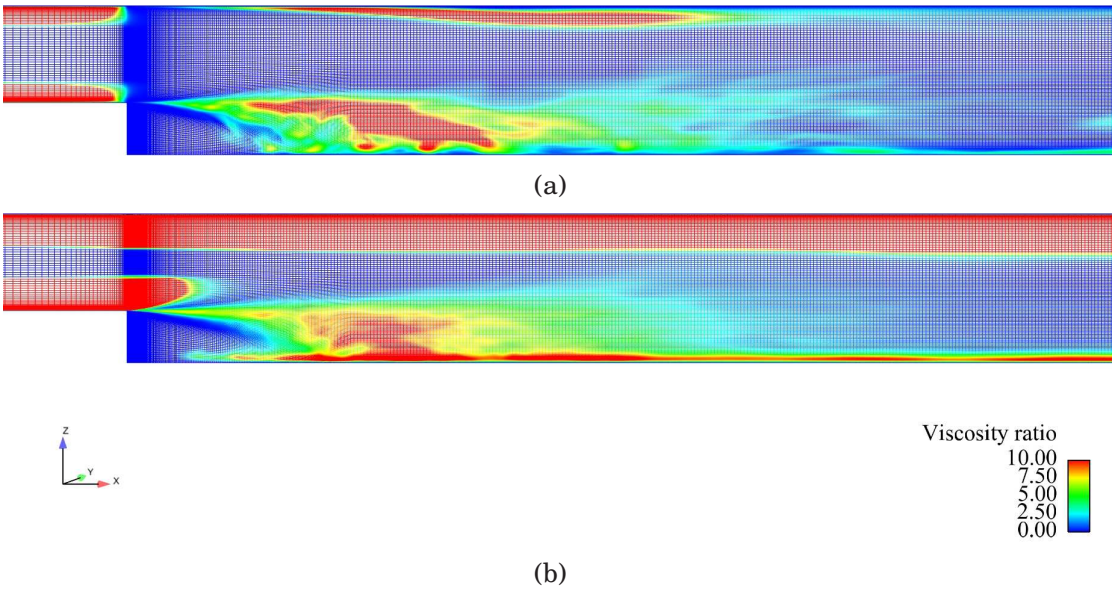

Figure 2.4: Viscosity ratio (grid is shown in the background). a) SA-DES. b) SA-DDES.

In Figs. 2.4(b) and 2.5(b), SA-DDES of the exact same flow is shown. It can be observed that due to the shielding function, the attached boundary layer at the top wall is protected, despite the fine grid above the step, and the RANS levels of eddy viscosity are maintained. Consequently, the modeled stresses are not depleted and there is no separation on the top wall. As mentioned earlier, the DDES approach has the tendency to worsen the gray area problem, which is shown in Fig. 2.4(b) in terms of high values of eddy viscosity reaching from the separation location at the step downstream into the early stage of the shear layer.

2.4.2 Gray area problem

The gray area problem of hybrid RANS/LES methods does appear often in practical applications. In the simplest way, it can be illustrated by a mixing layer flow, where two attached, RANS modeled upstream boundary layers merge at the trailing edge of a flat plate. With the regular HYB0 model, the shear layer exhibits two-dimensional tubes as shown in Fig. 2.6(a). Three-dimensional content develops after a considerable delay and remains rather weak. Figure 2.7(a) highlights that the missing three-dimensionality can be traced back to weak or non-existing momen-

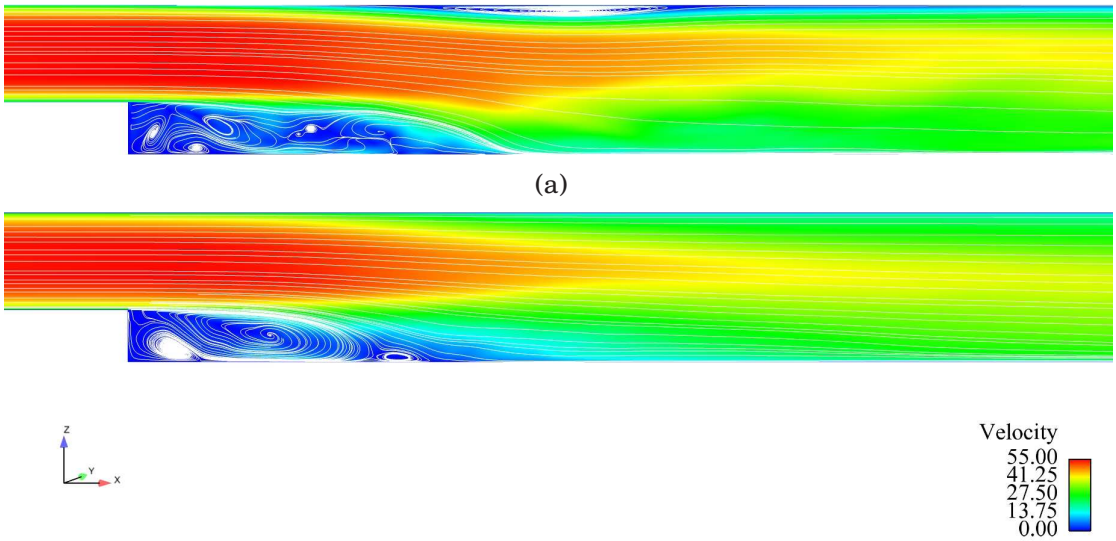

Figure 2.5: Mean velocity and streamlines. a) SA-DES. b) SA-DDES.

tum exchange in spanwise direction. In that sense, the computation is comparable to a two-dimensional RANS.

The situation can be considerably improved by employing the strategies mentioned in Section 2.3. In Fig. 2.6(b), the same mixing layer is shown for the HYB0 model with the additional energy backscatter term, $\tau_{L,ij}$ of Eq. (2.15). The backscatter is used for triggering the unstable modes of the shear layer. At the same time, the cubic root of the volume control, $\Delta = \Delta_{vol} = (\Delta x \Delta y \Delta z)^{1/3}$, is employed as the filter width in the LES region in order to reduce the levels of eddy viscosity. As a result of this treatment, fully three-dimensional turbulence is developed considerably faster. Moreover, it can be observed in Fig. 2.7(b) that the two modifications lead to an increase of momentum exchange closer to the trailing edge of the plate.

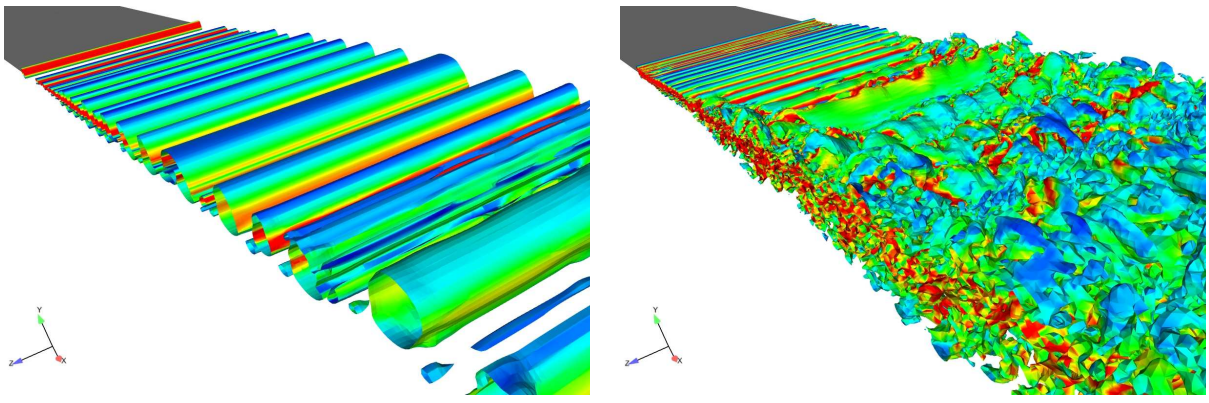

Figure 2.6: Comparing the turbulent structures from a) the standard HYB0 model and b) the HYB0 model with the additional backscatter term, $\tau_{L,ij}$ in Eq. (2.15), when using the cubic root of the control volume as the length scale in the LES region. Q-criterion colored by vorticity magnitude.

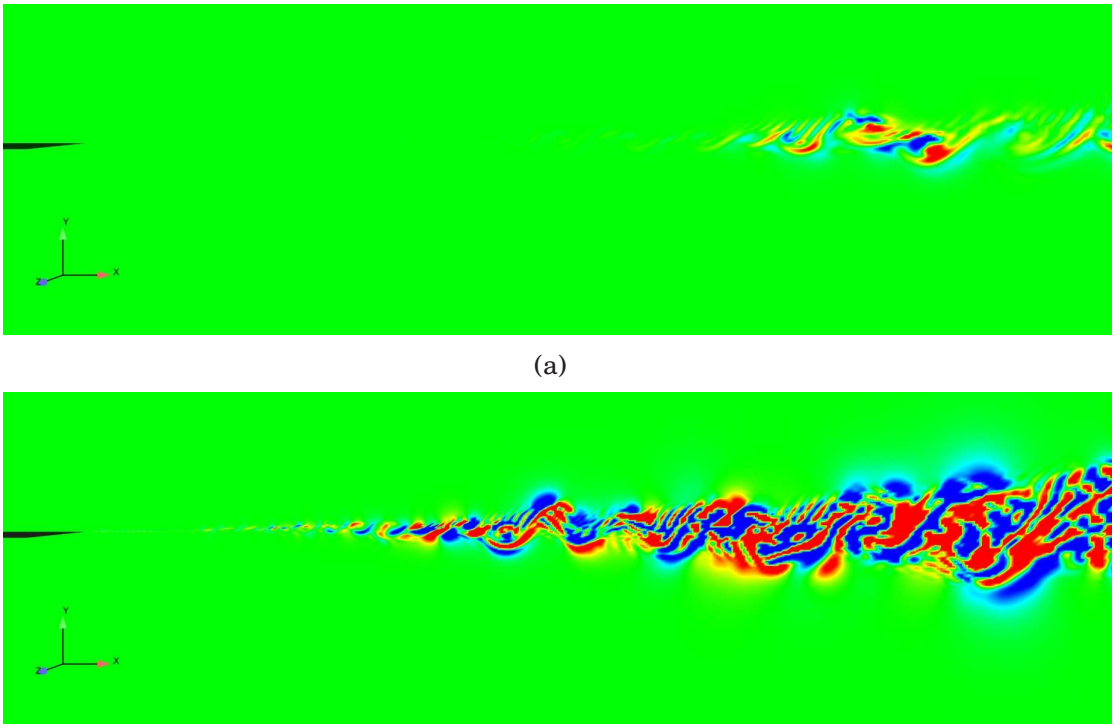

(a)

(b)

Figure 2.7: Comparing the spanwise velocity component, W, from a) the standard HYB0 model and b) the HYB0 model with the additional backscatter term, $\tau_{L,ij}$ in Eq. (2.15), when using the cubic root of the control volume as the length scale in the LES region.

Chapter 3

Acoustic analogies

In aeroacoustics it is of prime interest to predict the noise that is radiated to an observer located in the far-field. As the present case can be understood as the situation of a landing airplane, the observers are located at the ground below the airplane and are representative of residents close to an airport or ground personnel working at the airport. Obviously, the distance from the plane to the ground will decrease during the landing process, but a distance of a couple of hundreds of meters will be a reasonable estimate of the observer distance.

One way of predicting the far-field noise, is to include the observers into the computational domain and to use CFD for the prediction. This approach has initially been understood as Computational AeroAcoustics (CAA). However, acoustical disturbances are usually small compared to the flow fluctuations and in order not to dissipate them, the grid size has to be sufficiently fine all the way to the observer, leading to excessively large grids. As to avoid dissipation of the small disturbances, it is beneficial to invoke higher-order discretization schemes in the computation. Due to those requirements, it is not feasible nowadays to carry out far-field noise predictions solely based on CFD for cases of practical importance.

As of today, CAA is used more widely in terms of any kind of numerical noise prediction procedure. A popular strategy is to decouple the acoustic analysis from the flow computation. Firstly, a computation is carried out for providing the near-field flow solution, which captures all the noise sources stemming from non-linear flow effects. Acoustical analogies are then used for calculating the noise propagation to the far-field. The concept of acoustic analogies goes back to Lighthill, who proposed the first acoustic analogy in 1952 [64, 65]. In an acoustic analogy, the wave propagation is calculated based on the known solution to the wave equation for free space. Even though in CAA the unsteady data from the flow computation serves as input for the acoustic analogy, it should be noted that unsteady data from experiments could be used analogically. A brief insight into three commonly used acoustic analogies, namely the Kirchhoff surface integral method [23], the Ffowcs-Williams and Hawkings method [13, 24] for a stationary, permeable surface and the Curle method [25], is provided in the following. A more elaborate explanation of the derivation of the Kirchhoff and Ffowcs-Williams and Hawkings analogies based on generalized functions is given in Appendix A.

3.1 Kirchhoff surface integral method

As early as 1883, Kirchhoff's theory was published [66] and originally used for describing electromagnetic waves. Later on, Kirchhoff's formula has been exploited for acoustical problems on stationary and moving integral surfaces [23]. In the Kirchhoff surface integral method, a permeable control surface is assumed to enclose all acoustical sources. While all non-linear effects of the acoustical sources are found within the surface, outside of the surface, the flow satisfies the linear condition so that the homogeneous wave equation (Eq. (3.1)) is fulfilled.

$$\frac{1}{c_0^2}\frac{\partial^2 p'}{\partial t^2} - \nabla^2 p' \equiv \Box^2 p'(\vec{x},t) = 0 \tag{3.1}$$

where $\Box^2$ is referred to as the wave operator. Now, the pressure in Eq. (3.1) is replaced by a discontinuous function, such that it exists outside of the surface whereas it is set to zero inside the surface. With the help of generalized derivatives [23, 24], the generalized wave equation for the discontinuous pressure can be written as the Kirchhoff equation for a stationary surface [67]:

$$\bar{\Box}^2 p'(\vec{x},t) = -\frac{\partial p'}{\partial n}\delta(f) - \frac{\partial}{\partial x_i}[p' n_i \delta(f)] \tag{3.2}$$

In Eq. (3.2), generalized derivatives are denoted by an overbar, as in $\bar{\Box}^2$, $\delta(f)$ is the Dirac delta function, f denotes the surface and n_i denotes the components of the unit normal vector pointing outwards from the surface. A solution to Eq. (3.2) can be found via the free space Green function.

$$\begin{aligned} p'_K(\vec{x},t) = &\frac{1}{4\pi}\int_{f=0}\left(\frac{\cos\theta}{R^2}[p'(\vec{y},t)]_\tau - \frac{1}{R}\left[\frac{\partial p'(\vec{y},t)}{\partial n}\right]_\tau\right. \\ &\left. + \frac{\cos\theta}{c_0 R}\left[\frac{\partial p'(\vec{y},t)}{\partial \tau}\right]_\tau\right) dS \end{aligned} \tag{3.3}$$

where R denotes the distance to the observer, i.e. $R = |\vec{r}| = |\vec{x} - \vec{y}|$, $\cos\theta = (r_i/R)n_i$, c_0 is the speed of sound and $[\ ]_\tau$ indicates that the term is evaluated at retarded time, $\tau = t - R/c_0$. Yao et al. [21] propose to treat the three terms of Eq. (3.4) as individual surface integrals.

$$p'_{1,K}(\vec{x},t) = \frac{1}{4\pi}\int_{f=0}\left(\frac{\cos\theta}{R^2}[p'(\vec{y},t)]_\tau\right) dS \tag{3.4a}$$

$$p'_{2,K}(\vec{x},t) = -\frac{1}{4\pi}\int_{f=0}\left(\frac{1}{R}\left[\frac{\partial p'(\vec{y},t)}{\partial n}\right]_\tau\right) dS \tag{3.4b}$$

$$p'_{3,K}(\vec{x},t) = \frac{1}{4\pi}\int_{f=0}\left(\frac{\cos\theta}{c_0 R}\left[\frac{\partial p'(\vec{y},t)}{\partial \tau}\right]_\tau\right) dS \tag{3.4c}$$

The three terms represent the noise due to pressure fluctuations, the gradient and the time derivative of the pressure fluctuations, respectively. It is, of course, still true that the total noise is the summation of the terms in Eq. (3.4):

$$p'_{total,K} = p'_{1,K} + p'_{2,K} + p'_{3,K} \tag{3.5}$$

Particular care has to be taken when positioning the control surface in the domain. Since all acoustical sources have to be contained within the surface, so that the remainder of the flow field satisfies the homogeneous wave equation, the surface has to be located sufficiently far from the solid walls causing the disturbances. At the same time, CFD is used for predicting the flow field inside the surface. Due to the accuracy requirements of the CFD approach, it might not be affordable in terms of computational power, to place the Kirchhoff surface sufficiently far from the geometry. It should further be noted that different surfaces placed well outside the non-linear region of the flow should, theoretically, provide identical results [67].

3.2 Ffowcs-Williams and Hawkings' analogy

The acoustic analogy developed by Ffowcs-Williams and Hawkings [13] (FWH) was derived for solid surfaces moving at an arbitrary speed, v_n. Traditionally, the surface was assumed to be impermeable and to coincide with the solid wall of the geometry. Brentner and Farassat [24] derived a formulation of the FWH analogy for a permeable surface enclosing the acoustic sources, which made the approach similar to a Kirchhoff formulation. It is shown later that this is a fundamental advantage over the original formulation, because the volume integral, accounting for the quadrupole sources in the flow, can be neglected. Here, the special case of a stationary permeable surface is used, which can easily be extracted from Brentner's formulation [24] by setting $v_n = 0$.

Brentner and Farassat [24] rewrote the compressible Navier-Stokes equations with the help of generalized functions into a generalized wave equation with non-zero source terms, which is also referred to as the FWH-Equation (Eq. (3.6)).

$$\begin{aligned}\bar{\Box}^2 p'(\vec{x},t) = &- \frac{\partial}{\partial x_i}[(p'\delta_{ij} + \rho u_i u_j) n_j \delta(f)] \\ &+ \frac{\partial}{\partial t}[\rho u_j n_j \delta(f)] \\ &+ \frac{\bar{\partial}^2}{\partial x_i x_j}[T_{ij} H(f)]\end{aligned} \tag{3.6}$$

In the above equation, $T_{ij} = [(p' - \rho' c_0^2)\delta_{ij} - \tau_{ij} + \rho u_i u_j]$ is the Lighthill tensor [64, 65], δ_{ij} is the Kronecker delta and $H(f)$ is the Heaviside function. Acoustical sources enclosed by the surface contribute to the sound only through the surface terms (first and second term on the right-hand side of Eq. (3.6)). The third term in Eq. (3.6) is a volume term, which accounts for sources outside the surface. It was described earlier, that when using the Kirchhoff method, we assume the surface to enclose the entire core flow region and hence all acoustical sources. Owing to this assumption, it can be seen that the volume term is insignificant for the FWH formulation on an permeable surface. As mentioned earlier, this is an advantage over the original formulation of the FWH equation for a solid surface, because the costly calculation of the volume integral becomes redundant. Moreover, it should be noted here that a principal advantage of the FWH method over the Kirchhoff method is that the integral surface not necessarily needs to enclose all turbulence. A location closer to the solid walls can be used, which makes the entire CFD computation less costly.

However, this increases the error made by neglecting the volume integral term. A solution to Eq. (3.6) can be found, once again, based on Green's function for free space.

$$\begin{aligned} p'_F(\vec{x},t) = &- \frac{1}{4\pi}\frac{\partial}{\partial x_i}\int_{f=0}\left(\frac{1}{R}[p'\delta_{ij}+\rho u_i u_j]_\tau n_j\right)dS \\ &+ \frac{1}{4\pi}\frac{\partial}{\partial t}\int_{f=0}\left(\frac{1}{R}[\rho u_i n_j]_\tau\right)dS \end{aligned} \tag{3.7}$$

The above solution to the FWH equation, is the one originally derived for solid surfaces, when neglecting the volume integral. In this formulation, the first and second integral can directly be understood in physical terms as the loading and the thickness noise, respectively [68, 24]. When using a permeable surface, as in the present case, the terms lose their physical meaning and hence it is legitimate to write them as individual integrals as exercised by Yao et al. in [21]. In Eq. (3.8), it is then possible to interpret the three terms as the perturbations of pressure, momentum and mass through the surface, respectively.

$$p'_{1,F}(\vec{x},t) = \frac{1}{4\pi}\int_{f=0}\left(\frac{1}{R}\cos\theta\left[\left\{\frac{1}{c_0}\frac{\partial}{\partial\tau}+\frac{1}{R}\right\}p'\right]_\tau\right)dS \tag{3.8a}$$

$$p'_{2,F}(\vec{x},t) = \frac{1}{4\pi}\int_{f=0}\left(\frac{1}{R}\lambda_{ij}\left[\left\{\frac{1}{c_0}\frac{\partial}{\partial\tau}+\frac{1}{R}\right\}(\rho u_i u_j)\right]_\tau\right)dS \tag{3.8b}$$

$$p'_{3,F}(\vec{x},t) = \frac{1}{4\pi}\int_{f=0}\left(\frac{1}{R}n_j\left[\frac{\partial}{\partial\tau}(\rho u_j)\right]_\tau\right)dS \tag{3.8c}$$

where $\lambda_{ij} = (r_i/R)n_j$.

3.3 Curle's analogy

Curle's analogy can be regarded as a generalization of Lighthill's analogy [64, 65] in the presence of stationary solid walls. It is possible to derive the Curle equation analogically to Eq. (3.6). Introducing generalized variables into the compressible Navier-Stokes equations and rewriting them in terms of a wave equation with non-zero source terms, leads to the following:

$$\begin{aligned} \bar{\Box}^2 p'(\vec{x},t) = &- \frac{\partial}{\partial x_i}[p' n_i \delta(f)] \\ &+ \frac{\bar{\partial}^2}{\partial x_i x_j}[T_{ij}H(f)] \end{aligned} \tag{3.9}$$

Obviously, Eq. (3.9) is identical with the FWH equation, if a stationary solid surface is regarded in Eq. (3.6). A stationary, solid surface in the FWH method means that $u_i = u_j = 0$, which makes that Eq. (3.6) directly returns to Eq. (3.9). The solution to the Curle equation is given by the free space Green function as:

$$\begin{aligned} p'_C(\vec{x},t) = &- \frac{1}{4\pi}\frac{\partial}{\partial x_i}\int_{f=0}\left(\frac{1}{R}[p']_\tau n_i\right)dS \\ &+ \frac{1}{4\pi}\frac{\bar{\partial}^2}{\partial x_i x_j}\int_V\left(\frac{1}{R}[T_{ij}]_\tau\right)dV \end{aligned} \tag{3.10}$$

In Eq. (3.10), the surface integral stands for the pressure fluctuations on the solid wall due to the turbulent boundary layer. The second term represents the impact on the solid surface of the sound waves stemming from the quadrupoles in the flow field. Since only the pressure perturbations are of interest in this study, the volume integral in Eq. (3.10) is disregarded and the total noise for Curle's method can be obtained in the form presented by Yao and co-workers [20, 21]:

$$p'_C(\vec{x},t) = \frac{1}{4\pi}\int_{f=0}\left(\frac{1}{R}\cos\theta\left[\left\{\frac{1}{c_0}\frac{\partial}{\partial\tau}+\frac{1}{R}\right\}p'\right]_\tau\right)dS \tag{3.11}$$

Now, it becomes clear that Eq. (3.11) is the same as Eq. (3.8a) in the present formulation of the FWH approach.

Chapter 4

F15 high-lift airfoil

From a cut through the high-lift wing of a generic short to medium range aircraft with twin engines, as described in [5], a two-dimensional model of the three-element airfoil is obtained. The geometry is displayed in Fig. 4.1. It can be seen that a leading edge slat and a trailing edge flap are deployed from the main wing element. As compared to the clean wing, the slat and flap are deflected downwards by $28.8°$ and $38.3°$, respectively. The geometrical layout is representative of that of a landing airplane. From a manufacturing point of view, all of the three airfoil elements have to exhibit blunt trailing edges. This is accounted for in the computations at all trailing edges, except for the slat cusp, which is artificially sharpened.

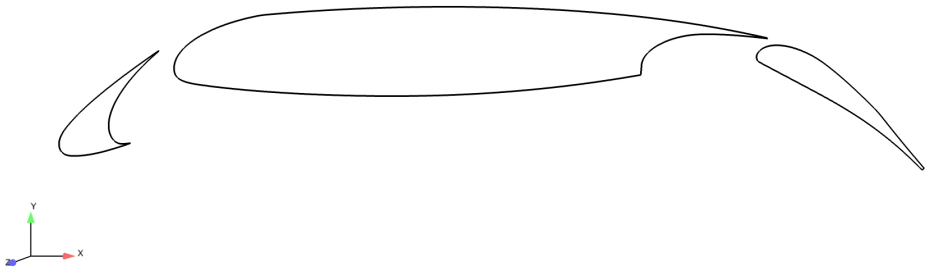

Figure 4.1: Geometrical definition of the airfoil with leading edge slat and trailing edge flap.

Experimental investigations on the F15 high-lift airfoil have been performed by Wild [5, 6] within the framework of the project LEISA (Low noise Exposing Integrated design for Start and Approach), which was carried out at the German Aerospace Center, DLR. The main focus of the studies in this project was the investigation of the airframe noise sources and the influence of the elements orientations on the aerodynamic and aeroacoustic properties. From that experimental campaign, the surface pressure distribution of all three elements is available for validation purposes.

In the EU project ATAAC (Advanced Turbulence Simulation for Aerodynamic Application Challenges), the DLR F15 airfoil was introduced as a numerical test case. The test case was classified as an ”Application Challenge” within the project, owing to its resemblance of an industrial application. Due to the fact that several

fundamental flow situations are present at the same time, such as free shear layers, laminar to turbulent boundary layer transition, confluence and interaction of boundary layers and wakes, the case can be considered challenging from a turbulence modeling point of view. Furthermore, the turbulence modeling approaches often are optimized for treating one of the above mentioned fundamental cases only and hence it can be seen as an additional challenge to combine accurate predictive behavior in one single method. The inherent characteristic of high-lift devices to generate airframe noise makes the present test case predestined for the evaluation of CAA tools.

During the course of this work, numerous computations were performed on different grids and with different objectives. In Table 4.1 an overview is given over the steady, two-dimensional RANS computations. The findings of those simulations are summarized in a technical report [69]. For the hybrid RANS/LES computations, only global approaches were considered and a corresponding overview is presented in Table 4.2. Cases H1 – H4 are summarized in Paper I [70]. Cases H5 and H6 are presented in Paper II [71]. Since case H6 from Table 4.2 is considered the most advanced one and the other cases are similar, the following description refers to case H6, unless otherwise stated.

Table 4.1: Information about the RANS computations

Case	Grid	N $[10^6]$	Transition	AoA $[^\circ]$	Model
R1	orig. (2D)	0.2	FT[c]/Trans.[d]	5, 6, 7	SA [e]
R2	orig. (2D)	0.2	FT[c]/Trans.[d]	5, 6, 7	BSL $k-\omega$[f]
R3	orig. (2D)	0.2	FT[c]/Trans.[d]	5, 6, 7	LRN $k-\omega$[g]
R4	orig. (2D)	0.2	FT[c]/Trans.[d]	5, 6, 7	SST $k-\omega$ [h]
R5	orig. (2D)	0.2	FT[c]/Trans.[d]	5, 6, 7	PDH LRN $k-\omega$[i]

[c] FT = Fully turbulent simulation
[d] Trans. = Transition location specified
[e] SA = Spalart-Allmaras model [46]
[f] BSL $k-\omega$ = Baseline Wilcox $k-\omega$ model [72]
[g] LRN $k-\omega$ = Low Reynolds Number Wilcox $k-\omega$ model [73]
[h] SST $k-\omega$ = Menter SST model [74, 29]
[i] PDH LRN $k-\omega$ = Peng-Davidson-Holmberg Low Reynolds Number $k-\omega$ model [75]

Table 4.2: Information about the hybrid RANS/LES computations

Case	Grid	N $[10^6]$	$\Delta x/C$	L_z	$\Delta z/C$	Δt $[s]$	Model
H1	orig.	8	0.0015	$8\%\ C$	0.002	4e-5	SA-DES
H2	orig.	8	0.0015	$8\%\ C$	0.002	4e-5	HYB0
H3	orig.	8	0.0015	$8\%\ C$	0.002	2e-5	HYB0
H4	orig.	16	0.0015	$16\%\ C$	0.002	2e-5	HYB0
H5	orig.	32	0.0015	$16\%\ C$	0.001	2e-5	HYB0
H6	ref.[j]	32	0.0005	$16\%\ C$	0.001	5e-6	HYB0

[j] ref. = refined

4.1 Numerical method

All computations were performed with the finite-volume flow solver Edge, developed by FOI (Swedish Defense Research Agency) [76, 77]. It solves the compressible Navier-Stokes equations on unstructured grids with arbitrary elements. For the unsteady computations, an implicit time integration scheme with 100 sub-iterations was used, which ensured that the inner residuals decreased by at least two orders of magnitude. In order to speed up convergence behavior, an agglomeration multi grid technique alongside with implicit residual smoothing was employed. The spatial discretization is based on a second-order accurate central scheme with artificial dissipation.

4.2 Test case description

The three-element airfoil, as shown in Fig. 4.1, is computed at free flight conditions. That means that no restrictions through wind tunnel walls are influencing the simulation and that the far-field boundaries are sufficiently far from the airfoil. In this case, the far-field boundary is located at $100C$ from the airfoil, with C being the stowed chord length. An unstructured grid of hybrid nature has been used for the computations. The near-wall region and ideally the boundary layers on all elements are treated with rectangular cells, while the off-wall region is treated with triangular cells. As the geometry is essentially two-dimensional, the grid is generated in the $x - y$ plane first. A close-up of the grid around the slat and the flap is depicted in Fig. 4.2. In order to create three-dimensionality, the two-dimensional grid slice is extruded equidistantly in spanwise direction for $16\%C$. The use of 160 grid cells in spanwise direction leads then to a spanwise grid resolution of $\Delta z/C = 0.001$ and a total number of grid nodes of about 32×10^6. Note, that the spanwise grid spacing is double the characteristic grid spacing, $\Delta x/C = 0.0005$, in the slat cove. In spanwise direction, periodic boundary conditions were employed.

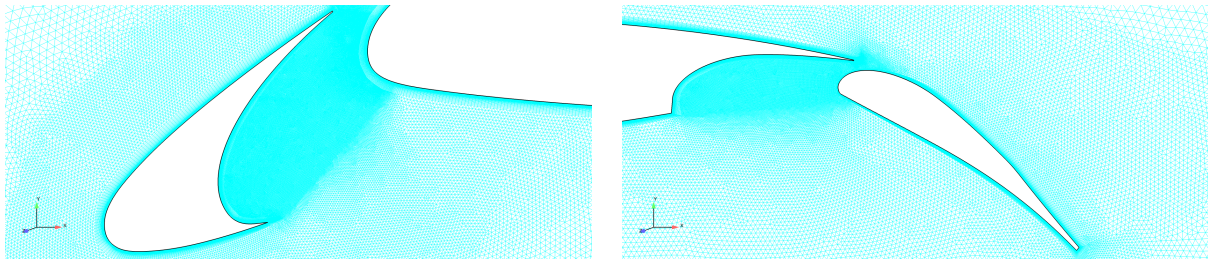

(a) (b)

Figure 4.2: Computational grid in the slat and flap region.

To enable noise propagation calculations using the acoustic analogies of Kirchhoff and Ffowcs-Williams and Hawkings, as described in Section 3, an integral control surface had to be included in the computational grid. This surface is stationary and permeable and its placement was based on the local vorticity magnitude. It was pointed out in Section 3.1 that the surface must enclose the entire core flow region, so that the assumption of a linear flow regime outside the surface is valid.

In order to ensure correct positioning of the surface, the vorticity magnitude was estimated from a precursor RANS computation. This is a procedure suggested by Yao and co-workers in [20]. The part of the surface enclosing the airfoil is displayed in Fig. 4.3. In streamwise direction, the surface stretches $6C$ downstream of the airfoil for capturing the effects of the wake behind the flap. The end of the surface in downstream direction is kept open in order to prevent numerical noise stemming from vortices passing the surface. At the surface the instantaneous flow quantities are sampled at each timestep.

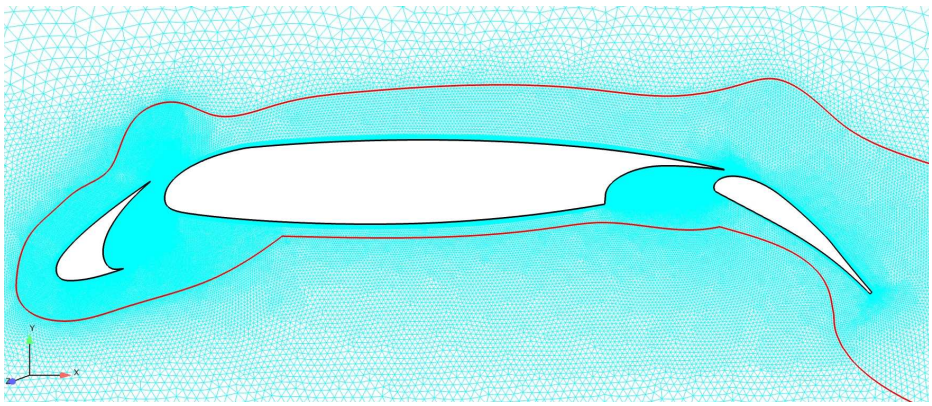

Figure 4.3: Integral surface for noise radiation calculations. The surface is represented by the red line.

The experiments were performed in a wind tunnel with a wall-to-wall model of the wing section at an AoA of $\alpha_{exp} = 7.05°$. On the wind tunnel side walls, an attached boundary layer was observed, which separated from the wall at the same streamwise location as the flow separates from the flap. Since the simulations are not taking into account the effect of the wind tunnel side walls, the AoA has to be corrected. These corrections were carried out by varying the AoA in steady, two-dimensional RANS computations in order to match the predicted and measured surface pressure distributions. A summary of those computations is given in [69]. Alongside with determining the corrected AoA, also the effect of various turbulence models and the prescription of laminar-turbulent boundary layer transition was investigated in the RANS simulations. As an outcome of the RANS studies, $\alpha_{corr} = 6°$ was chosen as the corrected AoA for the turbulence resolving simulations.

The freestream Mach number and chord-based Reynolds number are $M_\infty = 0.15$ and $Re_\infty = 2.1 \times 10^6$, respectively. Boundary layer transition locations are specified on all three elements of the airfoil. More specifically, the slat is kept laminar, whereas transition is specified on the suction sides of the wing and the flap as well as on the pressure side of the wing. The timestep size was chosen as $\Delta t = 5 \times 10^{-6}$ $[s]$ or $\Delta t = 0.00025683 C/U_\infty$ in dimensionless form, where U_∞ is the freestream velocity. Such a small timestep is employed to ensure a CFL number based on the maximum velocity of an acoustic wave, $(U_\infty + c_0)$, of CFL < 4 in the slat cove region.

Instantaneous and mean flow data has been extracted at the locations presented in Fig. 4.4.

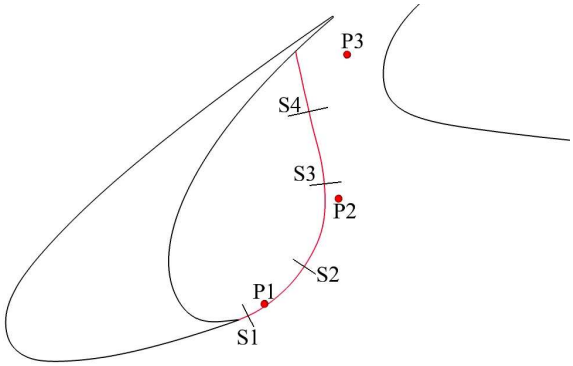

Figure 4.4: Locations for data extraction in the slat cove region. S1 – S4 are cross-sections of the shear layer, P1 – P3 are spanwise grid lines for plotting the two-point correlations and the red line along the shear layer is a spline, at which data was extracted.

Chapter 5

Summary of papers

5.1 Paper I

5.1.1 Motivation and work

In this paper, the DLR F15 three-element airfoil is investigated numerically using global hybrid RANS/LES modeling approaches. The influence of the hybrid RANS/LES model, the timestep size and the spanwise domain extent on the instantaneous and mean flow, along with near-field aeroacoustic properties is studied. An assessment of the minimum required spanwise domain extent is performed on the basis of spatial correlations. The near-field noise is studied in the slat cove region in terms of pressure fluctuations. Furthermore, the performance of the chosen hybrid RANS/LES approach is validated against experimental surface pressure data.

5.1.2 Results

The flow topology around the airfoil is displayed in Fig. 5.1 in terms of streamlines obtained from case H3. The flow stays attached on the lower and upper side of the slat until the slat cusp and the trailing edge, respectively. A recirculation region is formed within the slat cove, which is confined by the shear layer emanating from the slat cusp. Downstream of the slat trailing edge, the flows from the upper and lower sides merge. Even though not shown here, also around the main wing, all boundary layers are attached and a recirculating region is found in the cavity for the flap. Finally, on the suction side of the flap, flow separation can be observed.

The computations for the cases H1 – H5 from Table 4.2, were performed on the same grid. The only differences exist in the spanwise domain extent and the spanwise grid resolution. One of the goals with cases H3 – H5 was to determine the minimum spanwise domain extent required. The spanwise domain extent can be considered sufficient, once spatial correlations of pressure and velocity fluctuations drop to zero. This indicates that even the largest scales of the flow can be resolved within the domain. At locations P1 – P3 (see Fig. 4.4) the two-point correlations were calculated. It could be observed that the correlations were strong in all three locations, which suggests that even the large domain with a spanwise extent of $0.16C$ is not sufficient. This is explained partly with insufficient grid resolution in the $x-y$ plane and partly by the positioning of the sampling locations itself. Location P1 is

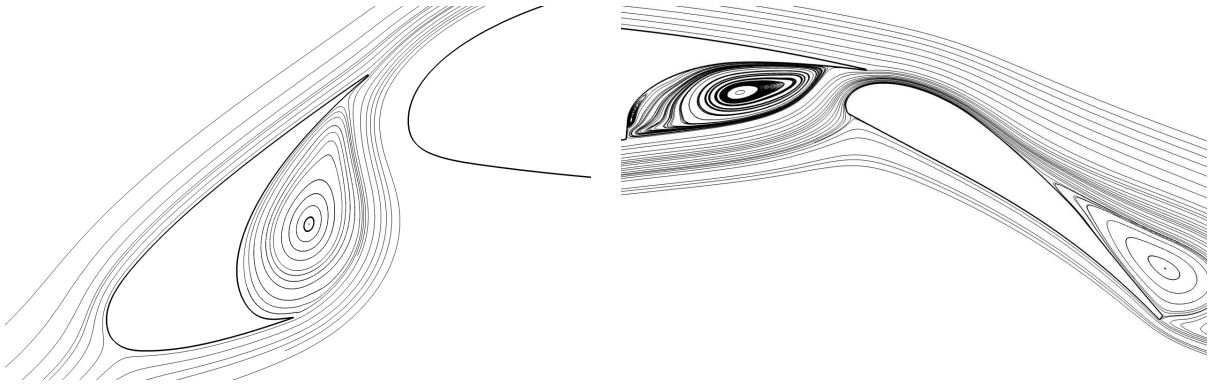

(a) slat (b) flap

Figure 5.1: Mean flow pattern around the high-lift configuration from computation H3. Visualized by streamlines.

situated right after the slat cusp in the initial shear layer and at least the correlations for the streamwise and vertical velocity fluctuations drop rapidly. However, locations P2 and P3 are situated next to the shear layer and in the gap between slat and wing, respectively. Those are locations with relatively weak turbulent content and due to the significant flow acceleration in those regions, the flow can even undergo relaminarization.

Furthermore, it was found from cases H1 – H5 that the slat shear layer was non-physically stable. The Kelvin-Helmholtz instabilities, which are inherent in shear layers could not be observed until half-way towards the impingement point on the lower slat trailing edge. The evolving structures were shown to be large. Undoubtedly, these large structures can be a further reason for the strong spanwise correlations observed. Grid refinement of the $x - y$ plane was expected to help diminishing the problem.

In terms of aeroacoustic analysis, broadbanded Sound Pressure Level (SPL) spectra, including several narrowbanded tonal peaks, were found at locations P1 – P3. The dominant tonal peak was associated to the fluctuating pressure in the shear layer. As the noise intensity increased towards location P3, it was concluded that the noise is generated in the vicinity of P3. This happens most likely at the impingement point of the shear layer on the lower slat trailing edge.

5.2 Paper II

5.2.1 Motivation and work

As Paper I indicated that the used grid in the $x - y$ plane was too coarse, a new grid with a refined slat cove region was designed. In order to enable far-field aeroacoustic analysis via the acoustic analogies of Kirchhoff and Ffowcs-Williams and Hawkings, also a permeable surface was included in the refined grid. Following the findings from Paper I, the spanwise domain extent and the resolution in spanwise direction were chosen to be $0.16C$ and $\Delta z/C = 0.001$, respectively.

In this paper, for the first time, three acoustic analogies are used for the predic-

tion of far-field noise of a three-element airfoil. Previously, quite some effort has been invested by the research community in the investigation of slat noise [14, 15, 4, 78]. Paper II, however, provides a study of the sound emitted by all three elements. Using Curle's analogy, also the emission behavior of the three elements can be explored separately.

5.2.2 Results

As shown in Fig. 5.2, the mean flow pattern does not change significantly, when using the new grid. The flow around slat and wing exhibit similar behavior as presented for case H3. Solely, the separation on the flap is predicted to be smaller in case H6, as compared to case H3 in Fig.5.1(b). Figure 5.3 displays iso-surfaces of the

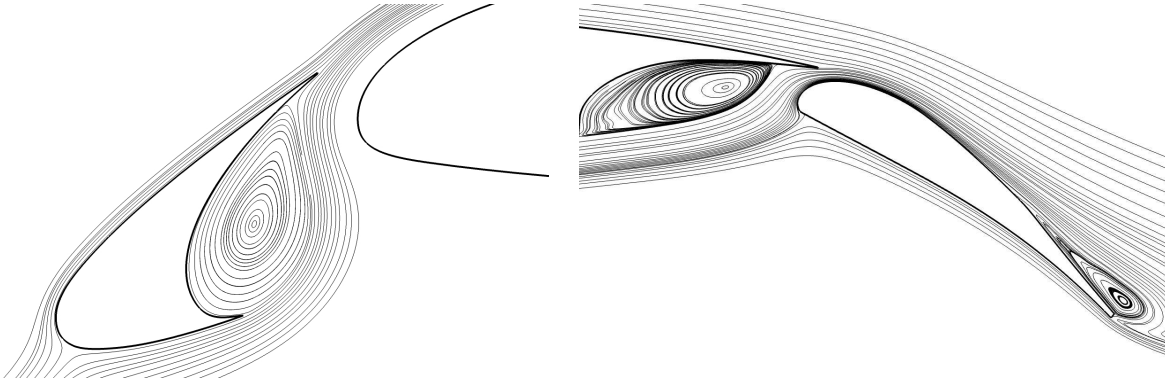

(a) slat (b) flap

Figure 5.2: Mean flow pattern around the high-lift configuration from computation H6. Visualized by streamlines.

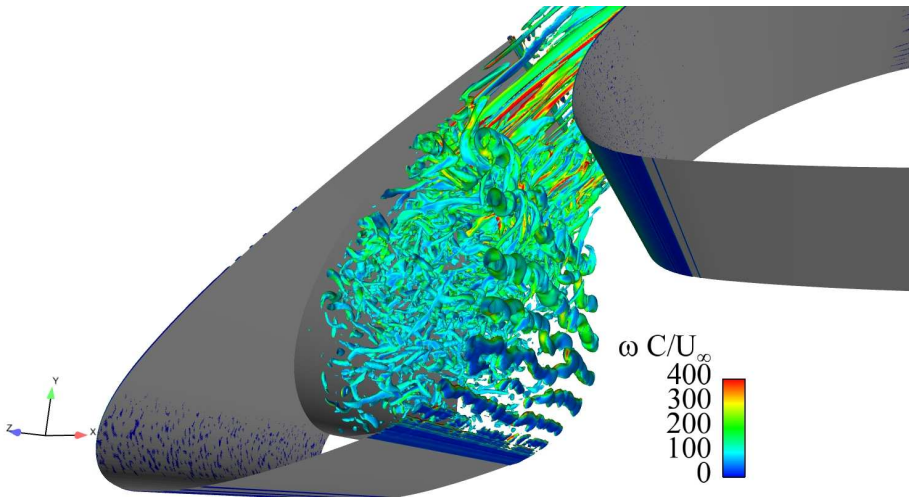

Figure 5.3: Iso-surfaces of the Q-invariant for the free shear layer emanating from the slat cusp for case H6. $\frac{QC^2}{U_\infty^2} = 5000$. Coloring by vorticity magnitude.

Q-criterion for the slat shear layer obtained on the refined grid. Almost immediately

downstream of the slat cusp, the shear layer exhibits Kelvin-Helmholtz instabilities, represented by the roll-up of coherent vortical structures in spanwise direction. However, the conversion of the coherent structures into fully three-dimensional turbulence occurs rather late. This is no longer attributable to insufficient grid resolution in the $x - y$ plane, but can rather be seen as a prime example of the gray area problem in hybrid RANS/LES methods. Its alleviation should be addressed in terms of turbulence modeling as indicated in Section 2.3.

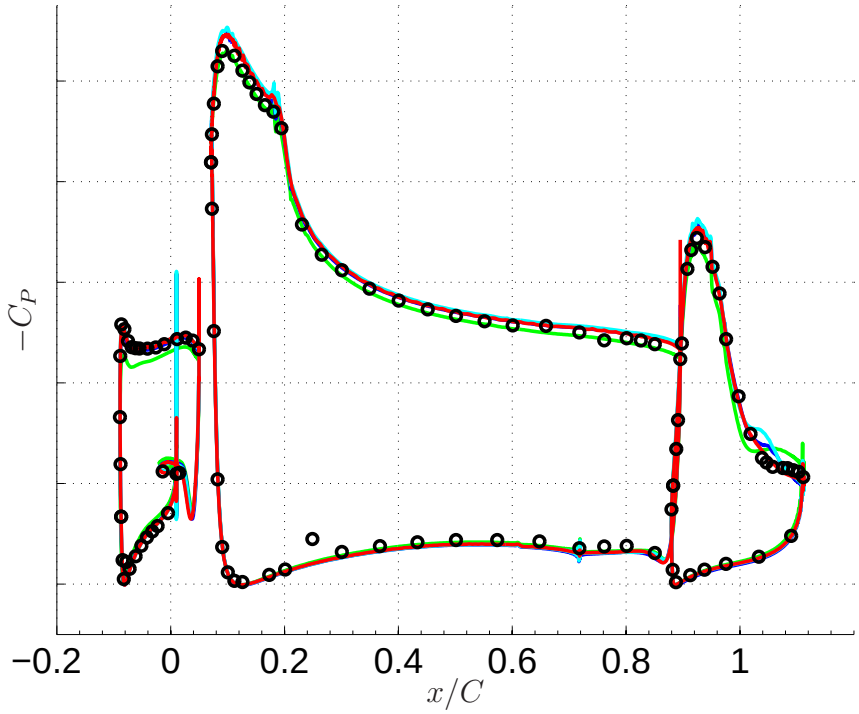

Figure 5.4: Mean pressure distribution for all elements. ——: Case H3, ——: Case H4, ——: Case H5, ——: Case H6. ○: Experiments. $\Delta C_P = 1$

From the experiments, surface pressure data was available for validation. A cross-comparison of cases H3 – H6 against these experimental data are given in Fig. 5.4 for all elements of the airfoil. Please note, that due to confidentiality the absolute pressure levels on the y-axis had to be omitted. It can be observed that case H3 yields the best result on the main wing, but deviates from the experiments on the slat and flap. Figure 5.5 provides a zoom-up for the slat and the flap. While the cases involving the large spanwise extent, i.e. cases H4 – H6, show results that are almost identical to each other and in excellent agreement with experiments on the slat, case H3 overpredicts the pressure on the suction side of the slat. On the flap, case H6 shows results superior to the other computations, as the separation is predicted in a better way. Cases H3 – H5 yield a plateau after separation. The differences in separation on the flap between cases H3 and H6 are consistent with the findings from Figs. 5.1(b) and 5.2(b).

To further highlight the superiority of case H6 over cases H3 – H5, the resolved turbulent kinetic energy is extracted along the shear layer following the spline in Fig. 4.4. Note, that case H5 uses the identical grid of cases H3 and H4, but with the finest spanwise resolution. It is hence assumed that case H5 is representative

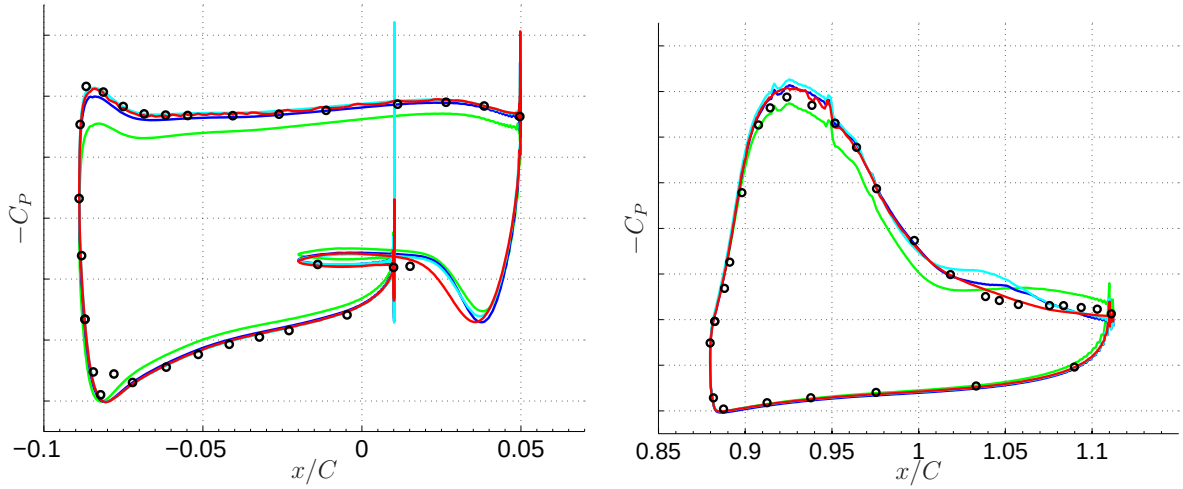

(a) slat (b) flap

Figure 5.5: Mean pressure distribution around slat and flap. ——: Case H3, ——: Case H4, ——: Case H5, ——: Case H6. ○: Experiments. $\Delta C_P = 1$

for the situation of cases H3 – H5, i.e. cases H3 and H4 are expected to perform worse. Indeed, it is evidenced by Fig. 5.6 that the levels of resolved turbulent kinetic energy obtained with case H6 exceed the ones obtained with case H5 along the entire shear layer. Note that the displayed turbulent kinetic energy is based on the normal stresses in the x- and y-directions only, i.e. $k_{uv} = \sqrt{\overline{u'u'} + \overline{v'v'}}$. This is done for the sake of comparability to experimental and numerical results in literature on similar high-lift airfoils. In fact, in the present case, k_{uv} does not differ significantly from k_{uvw} since the resolved turbulence in spanwise direction is weak, which was already expected from Fig. 5.3. Even though case H6 shows significantly higher resolved kinetic energy than case H5, Deck [17] reports levels as high as $k_{uv}/U_\infty^2 \approx 0.02$ in the initial shear layer. Further numerical [15] and experimental [79] studies on similar airfoils also found levels of around 2%. With a hybrid RANS/LES modeling approach adapted to the treatment of free shear layers, turbulent content could be resolved more quickly after separation and hence, the turbulent kinetic energy of H6 is expected to be more comparable to the aforementioned levels.

Also for case H6 the spanwise two-point correlations have been calculated. A comparison of case H6 and H5 is presented in Fig. 5.7. It can be seen that for all three locations along the shear layer, the correlations drop to lower values when the refined grid is used. Note, that the spanwise resolution and domain extent is the same in both computations displayed. One can then conclude that the spanwise correlations have significantly been influenced by the grid resolution in the $x - y$ plane.

As already mentioned above, the prediction of the noise radiation from the high-lift devices is an important issue and one of the major goals of this study. The instantaneous flow field has been sampled at each timestep at the permeable surface and at the solid walls of the airfoil. This enables the use of the three acoustic analogies described in Section 3. With the help of acoustic analogies, the noise could be radiated to a number of far-field observers. In total, 72 observers are located on a circle

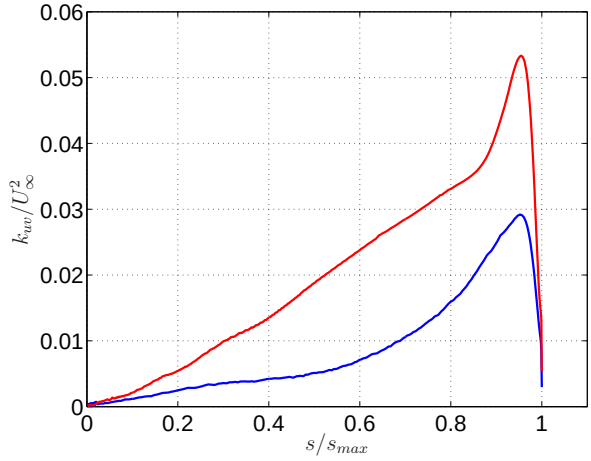

Figure 5.6: Development of the resolved turbulent kinetic energy, k_{uv}, along the slat shear layer. ——: Case H5, ——: Case H6. s/s_{max} denotes the position along the shear layer from the slat cusp.

with radius $300C$ around the airfoil, which should approximately be representative of the distance to a landing airplane. The axis orientations of the polar coordinate system used, are depicted in Fig. 5.8. The upstream and downstream directions are located at $\theta = 0°$ and $\theta = 180°$, respectively. The upward and downward directions become then $\theta = 90°$ and $\theta = 270°$. It should be noted that only the noise in the downward direction is of practical interest, as this part represents the noise radiated towards the population on the ground. All other angles are only included for comparability and completeness.

In Fig. 5.9(a), the directivity plots obtained by the three acoustic analogies are compared. It can be seen that the Curle method yields the lowest noise levels, which was to be expected, since only the pressure fluctuations on the solid surface of the airfoil are taken into account. The FWH method accounts for the influence of the quadrupole sources by the surface integrals, which explains the difference to the Curle method in which the quadrupole sources are neglected. The Kirchhoff method exhibits by far the highest noise levels. Figure 5.9(b) gives insight into the radiation behavior of the three elements. The slat and flap act as dipoles with emission maxima roughly in the directions perpendicular to their own orientation. The main wing does not exhibit a clear radiation pattern, but that might be due to the presence of two dipoles masking each other.

SPL plots are compared for the three acoustic analogies in the downward direction. All analogies yield broadbanded spectra with some narrowbanded tonal peaks. The strongest tonal peak is exhibited at $St \approx 2.8$ with adjacent peaks at $St \approx 0.95$, $St \approx 1.9$, $St \approx 3.6$ and $St \approx 4.5$. The frequency of the peaks is predicted fairly similar by all three acoustic analogies. From Fig. 5.9(a), one could expect that the Kirchhoff method would show by far the highest levels, but the spectra are shown to be rather similar. The part of the spectrum that makes the difference is the energy located at low frequencies, i.e. $St < 1$.

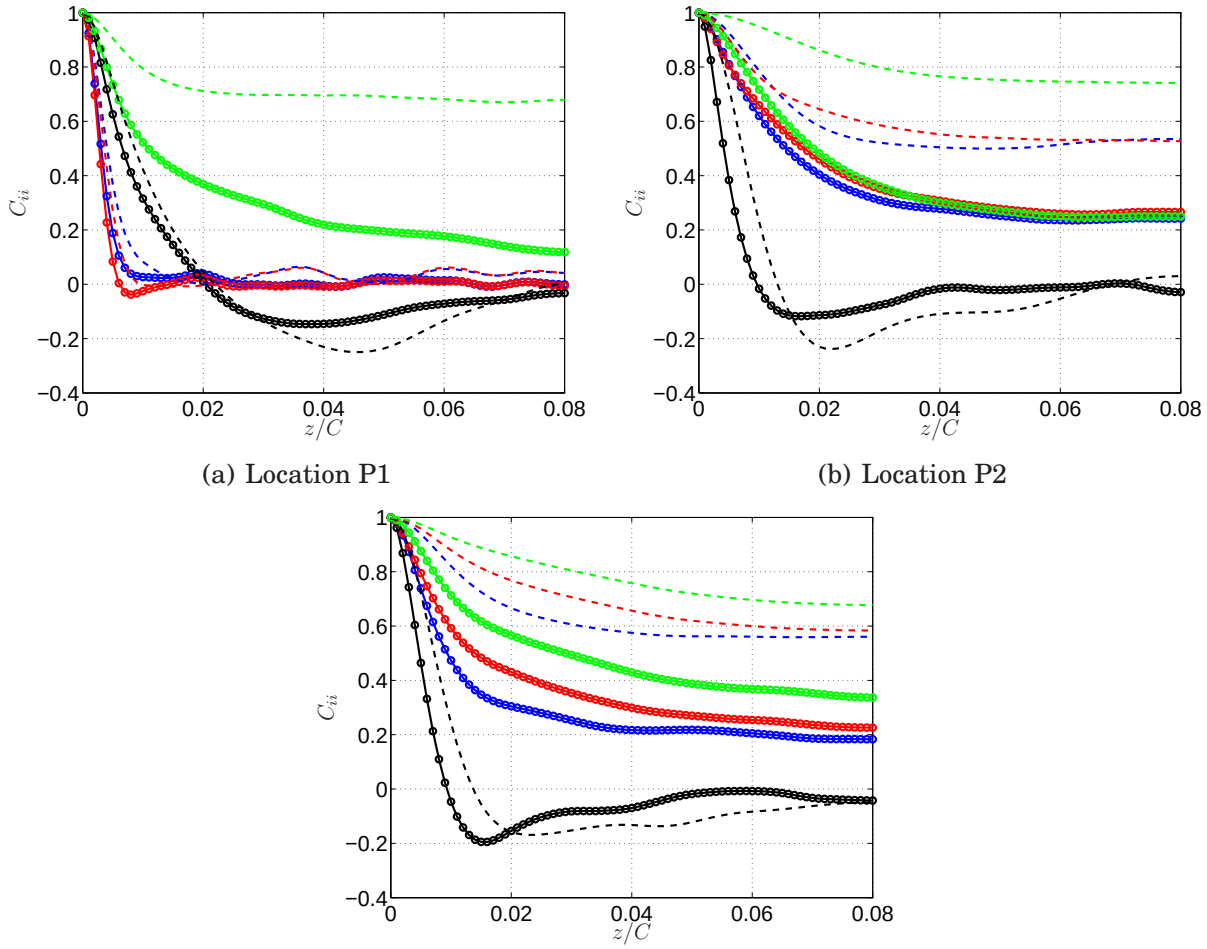

(a) Location P1

(b) Location P2

(c) Location P3

Figure 5.7: Spanwise two-point correlations in the slat cove region; dashed lines: Case H5; solid lines: Case H6, ——: $C_{uu,norm}$, ——: $C_{vv,norm}$, ——: $C_{ww,norm}$, ——: $C_{pp,norm}$. Markers on the lines indicate the spanwise resolution.

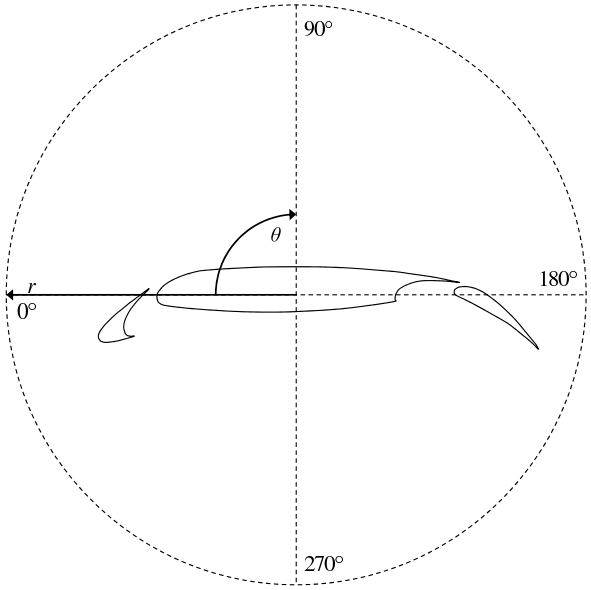

Figure 5.8: Polar coordinate-system

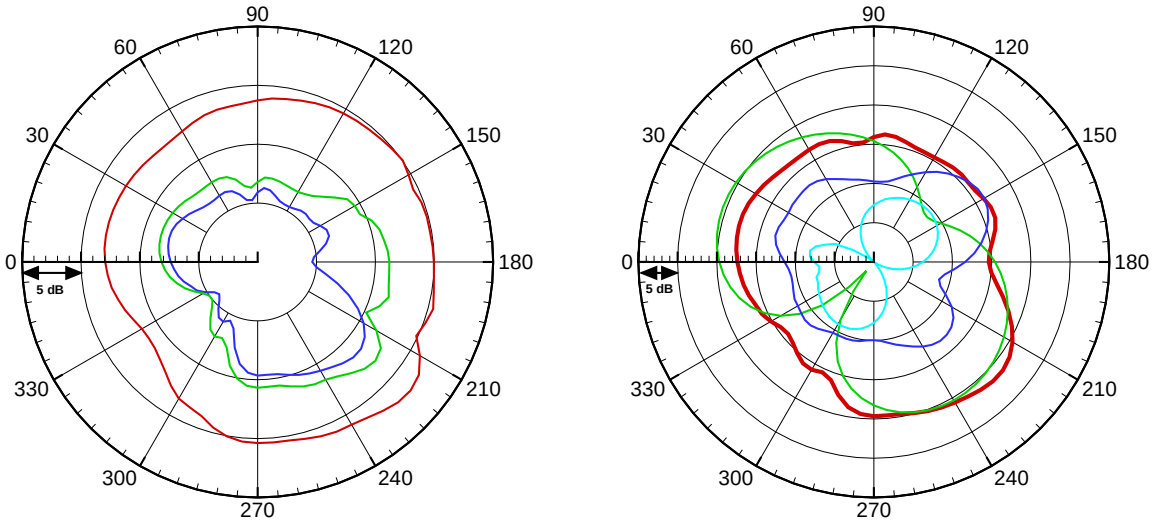

(a) all analogies

(b) Curle

Figure 5.9: a) OASPL for the three acoustic analogies. ——: Kirchhoff, ——: Curle, ——: FWH; b) OASPL for the Curle method. ——: $p'_{total,C}$, ——: $p'_{slat,C}$, ——: $p'_{wing,C}$, ——: $p'_{flap,C}$.

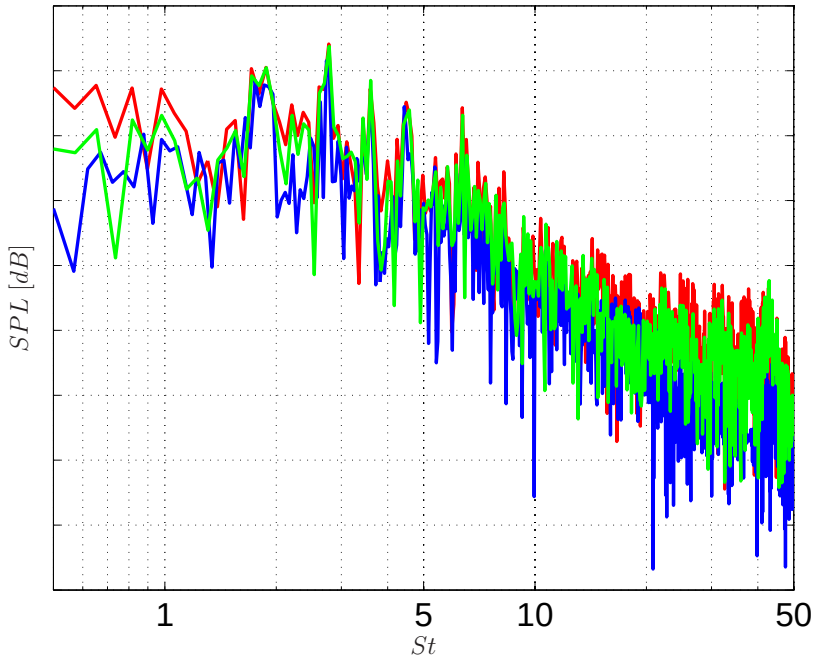

(a) $\theta = 270°$

Figure 5.10: Comparison of the SPL obtained with the three acoustic analogies, radiation in downward direction. ——: Kirchhoff, ——: Curle, ——: FWH. $\Delta SPL = 10\ [dB]$.

Chapter 6

Concluding remarks and future work

6.1 Conclusion

Global hybrid RANS/LES simulations were utilized for the computation of the turbulent flow around a three-element airfoil. The employed hybrid RANS/LES modeling approaches evidenced that turbulence resolving simulations are feasible for the complex flow of a high-lift system. The presented results are of unsteady nature and hence well beyond the capabilities of traditional steady RANS approaches. In order to ensure accurate results, the spanwise domain extent has to be chosen large enough. The study of the present case showed that a spanwise domain extent of $0.16C$ is sufficient. It was pointed out that the grid resolution in the $x-y$ plane plays an important role and should be chosen fine enough as to support turbulence resolving behavior of the chosen hybrid approach.

It was shown that the HYB0 model suffers from the gray area problem and that the issue is not fully redeemable with (reasonable) grid refinement. Even though the mean flow could be predicted well already with the original, coarse grid, the use of the refined grid increased the turbulence resolving capabilities of the HYB0 model considerably. Surface pressure distributions in excellent agreement with experiments could be reproduced, particularly for the slat.

The CAA strategy of using a hybrid RANS/LES simulation for predicting the unsteady flow and calculating the noise propagation to the far-field with the help of acoustic analogies has proved to be efficient. Predictions of far-field noise that would not be feasible based solely on CFD, were carried out and showed promising results. Due to the use of the permeable control surface, the amount of stored data could be reduced considerably. Results obtained with the three acoustical analogies are in good agreement with each other in terms of the frequencies at which tonal peaks are predicted. However, the noise levels obtained by the three analogies differ considerably. The Kirchhoff method predicts larger values than both the FWH and the Curle method. The deviations between the FWH and Curle methods are smaller and explainable through the differences in the formulations of the analogies. Using the Curle method, it could be shown that the slat and the flap emit noise in a dipole fashion. The radiation maxima are located roughly in the directions perpendicular

to their own orientations.

6.2 Future work

In the future, a hybrid RANS/LES computation making use of one or several improvements explained in Section 2.3 should be performed. This allows for capturing more physical aspects, especially due to the shear layers and it is beyond doubt that the far-field noise prediction would benefit from that. Once it is affordable in terms of computational power, it would be desirable to improve the grid resolution around the main wing and flap. Furthermore, it is recommendable to use higher-order spatial discretization schemes in order to reduce the numerical dissipation. For future validation purposes new experimental campaign would be invaluable. Besides far-field noise spectra at given observer locations, Particle Image Velocimetry (PIV) measurements should be conducted so that instantaneous and mean flow properties, as well as second order statistics (RMS) of the flow quantities, can be acquired.

Bibliography

[1] INTERNATIONAL CIVIL AVIATION ORGANIZATION. *Annex 16 to the Convention on International Civil Aviation, Volume 1 Aircraft Noise*. ICAO, 4th edition, 2005.

[2] NASA Facts. *Making Future Commercial Aircraft Quieter*. NASA, 1999. FS-1999-07-003-GRC.

[3] W. Dobrzynski, K. Nagakura, B. Gehlhar, and A. Buschbaum. Airframe Noise Studies on Wings with Deployed High-Lift Devices. In *4th AIAA/CEAS Aeroacoustics Conference*, Toulouse, France, 2-4 June 1998. AIAA paper 98-2337.

[4] W. Dobrzynski and M. Pott-Pollenske. Slat Noise Source Studies for FarField Noise Prediction. In *7th AIAA/CEAS Aeroacoustics Conference*, Maastricht, The Netherlands, 28-30 May 2001. AIAA paper 2001-2158.

[5] J. Wild, M. Pott-Pollenske, and B. Nagel. An integrated design approach for low noise exposing high-lift devices. In *3rd AIAA Flow Control Conference*, San Francisco, USA, 2006. AIAA paper 2006-2843.

[6] J. Wild, G. Wichmann, F. Haucke, I. Peltzer, and P. Scholz. Large scale separation flow control experiments within the German Flow Control Network. In *47th AIAA Aerospace Sciences Meeting*, Orlando, USA, 2009. AIAA paper 2009-0530.

[7] B.L. Storms, J.A. Hayes, J.C. Ross, and P.J. Moriarty. Aeroacoustic measurements of slat noise on a three-dimensional high-lift system. In *5th AIAA/CEAS Aeroacoustics Conference*, Greater Seattle, USA, 10-12 May 1999. AIAA paper 99-1957.

[8] W. Dobrzynski, B. Gehlhar, and H. Buchholz. Model and full scale high-lift wing wind tunnel experiments dedicated to airframe noise reduction. *Aerospace Science and Technology*, 5:27–33, 2001.

[9] Y.P. Guo and M.C. Joshi. Noise Characteristics of Aircraft High-Lift Systems. *AIAA Journal*, 41:1247–1256, 2003.

[10] L.C. Chow, K. Mau, and H. Remy. Landing Gears and High Lift Devices Airframe Noise Research. In *8th AIAA/CEAS Aeroacoustics Conference and Exhibit*, Breckenridge, USA, 17-19 June 2002. AIAA paper 2002-2408.

[11] M.R. Khorrami, M.E. Berkman, and M. Choudhari. Unsteady Flow Computations of a Slat with a Blunt Trailing Edge. *AIAA Journal*, 38:2050–2058, 2000.

[12] B.A. Singer, D.P. Lockard, and K.S. Brentner. Computational Aeroacoustic Analysis of Slat Trailing-Edge Flow. *AIAA Journal*, 38:1558–1564, 2000.

[13] J.E. Ffowcs-Williams and D.L. Hawkings. Sound Generation by Turbulence and Surfaces in Arbitrary Motion. *Philosophical Transactions of the Royal Society*, 264:321–342, 1969.

[14] M.M. Choudhari and M.R. Khorrami. Effect of Three-Dimensional Shear-Layer Structures on Slat Cove Unsteadiness. *AIAA Journal*, 45:2174–2186, 2007.

[15] D.P. Lockard and M.M. Choudhari. Noise Radiation from a Leading-Edge Slat. In *15th AIAA Aeroacoustics Conference*, Miami, USA, 11-13 May 2009. AIAA paper 2009-3101.

[16] S. Deck. Zonal-Detached-Eddy Simulation of the Flow Around a High-Lift Configuration. *AIAA Journal*, 43:2372–2384, 2005.

[17] S. Deck. Recent improvements in the Zonal Detached Eddy Simulation (ZDES) formulation. *Theor. Comput. Fluid Dyn.*, pages 1–28, 2011. DOI 10.1007/s00162-011-0240-z.

[18] M. Terracol, E. Manoha, C. Herrero, E. Labourasse, S. Redonnet, and P. Sagaut. Hybrid methods for airframe noise numerical prediction. *Theor. Comput. Fluid Dyn.*, 19:197–227, 2005. DOI 10.1007/s00162-005-0165-5.

[19] U. Michel, D. Eschricht, B. Greschner, T. Knacke, C. Mockett, and F. Thiele. Advanced DES Methods and Their Application to Aeroacoustics. In S.-H. Peng et al., editor, *Progress in Hybrid RANS-LES Modelling, NNFM*, volume 111, pages 59–76. Springer, 2010.

[20] H.-D. Yao, L.-E. Eriksson, L. Davidson, O. Grundestam, S.-H. Peng, and P.E. Eliasson. Aeroacoustic Assessment of Conceptual Low-Noise High-Lift Wing Configurations. In *50th AIAA Aerospace Sciences Meeting incl. the New Horizons Forum and Aerospace Exposition*, Nashville, USA, 09-12 January 2012. AIAA paper 2012-0383.

[21] H.-D. Yao, L. Davidson, L.-E. Eriksson, O. Grundestam, S.-H. Peng, and P.E. Eliasson. Surface Integral Analogy Approaches to Computing Noise Generated by a 3D High-Lift Wing Configuration. In *50th AIAA Aerospace Sciences Meeting incl. the New Horizons Forum and Aerospace Exposition*, Nashville, USA, 09-12 January 2012. AIAA paper 2012-0386.

[22] B.A. Singer and Y. Guo. Development of Computational Aeroacoustics Tools for Airframe Noise Calculations. *International Journal of Computational Fluid Dynamics*, 18:455–469, 2004.

[23] F. Farassat and M.K. Myers. Extension of Kirchhoff's Formula to Radiation from Moving Surfaces. *Journal of Sound and Vibration*, 123:451–460, 1988.

[24] K.S. Brentner and F. Farassat. Modeling aerodynamically generated sound of helicopter rotors. *Progress in Aerospace Sciences*, 39:83–120, 2003.

[25] N. Curle. The influence of solid boundaries upon aerodynamic sound. *Proceedings of the Royal Society of London. Series A, Mathematical and Physical Sciences*, 231:505–514, 1955.

[26] P.R. Spalart. Strategies for turbulence modelling and simulations. *International Journal of Fluid Flow*, 21:252–263, 2000.

[27] P.R. Spalart, W-H. Jou, M. Strelets, and S.R. Allmaras. Comments on the Feasibility of LES for Wings and on a Hybrid RANS/LES Approach. In *Proceedings of the First AFOSR International Conference on DNS/LES*, pages 137–147, Ruston, USA, 1997. Greyden Press.

[28] F.R. Menter and M. Kuntz. Adaption of eddy-viscosity turbulence models to unsteady separated flow behind vehicles. In R. McCallen, F. Browand, and J. Ross, editors, *Symposium on the aerodynamics of heavy vehicles: trucks, buses and trains.*, Monterey, USA, 2-6 December 2002. Springer.

[29] F.R. Menter, M. Kuntz, and R. Langtry. Ten Years of Industrial Experience with the SST Turbulence Model. In *Turbulence, Heat and Mass Transfer 4*, Antalya, Turkey, 2003. Begell House.

[30] S. Deck. Numerical Simulation of Transonic Buffet over a Supercritical Airfoil. *AIAA Journal*, 43:1556–1566, 2005.

[31] P.R. Spalart, S. Deck, M.L. Shur, K.D. Squires, M.Kh. Strelets, and A. Travin. A new Version of Detached-Eddy Simulation, resistant to Ambiguous Grid Densities. *Theor. Comput. Fluid Dyn.*, 20:181–195, 2006.

[32] P.R. Spalart. Detached-Eddy Simulation. *Annual Reviews of Fluid Mechanics*, 41:181–202, 2009.

[33] L. Davidson and S.-H. Peng. A hybrid LES-RANS model based on a one-equation SGS model and a two-equation $k - \omega$ model. In E. Lindborg, A. Johansson, J. Eaton, J. Humphrey, N. Kasagi, M. Leschziner, and M. Sommerfeld, editors, *Proceedings of 2nd International Symposium on Turbulence and Shear Flow Phenomena*, volume 2, pages 175–180, Stockholm, Sweden, 2001.

[34] L. Davidson and S. Dahlstrom̈. Hybrid LES-RANS: an approach to make LES applicable at high Reynolds number. *International Journal of Computational Fluid Dynamics*, 19:415–427, 2005.

[35] L. Davidson and M. Billson. Hybrid LES-RANS using synthesized turbulent fluctuations for forcing in the interface region. *International Journal of Heat and Fluid Flow*, 27:1028–1042, 2006.

[36] P.R. Spalart. Direct simulation of a turbulent boundary layer up to $R_\theta = 1410$. *Journal of Fluid Mechanics*, 187:61–98, 1988.

[37] T.S. Lund, X. Wu, and K.D. Squires. Generation of Turbulent Inflow Data for Spatially-Developing Boundary Layer Simulations. *Journal of Computational Physics*, 140:233–258, 1998.

[38] M.L. Shur, P.R. Spalart, and M.Kh. Strelets. Noise prediction for increasingly complex jets. Part I: Methods and tests. *International Journal of Aeroacoustics*, 4:213–246, 2005.

[39] P.J. Morris, L.N. Long, A. Bangalore, and Q. Wang. A Parallel Three-Dimensional Computational Aeroacoustics Method Using Nonlinear Disturbance Equations. *Journal of Computational Physics*, 133:56–74, 1997.

[40] E. Labourasse and P. Sagaut. Reconstruction of Turbulent Fluctuations Using a Hybrid RANS/LES Approach. *Journal of Computational Physics*, 182:301–336, 2002.

[41] M. Terracol. A Zonal RANS/LES Approach for Noise Sources Prediction. In W. Rodi, editor, *Flow, Turbulence and Combustion: Special Issue: ERCOFTAC International Symposium on Engineering Turbulence Modelling and Measurements - ETMM6*, volume 77, pages 161–184. Springer, 2012.

[42] S.S. Girimaji. Partially-Averaged Navier-Stokes Model for Turbulence: A Reynolds-Averaged Navier-Stokes to Direct Numerical Simulation Bridging Method. *Journal of Applied Mechanics*, 73:652–669, 2006.

[43] J.M. Ma, S.-H. Peng, L. Davidson, and F.J. Wang. A Low Reynolds Number Variant of Partially-Averaged Navier-Stokes Model for Turbulence. *International Journal of Heat and Fluid Flow*, 32:413–421, 2011.

[44] L. Davidson. A NEW APPROACH OF ZONAL HYBRID RANS-LES BASED ON A TWO-EQUATION k-ε MODEL. In *ETMM9: 9th International ERCOFTAC Symposium on Engineering*, Thessaloniki, Greece, 6-8 June 2012.

[45] M.L. Shur, P.R. Spalart, M.Kh. Strelets, and A.K. Travin. A hybrid RANS-LES approach with delayed-DES and wall-modelled LES capabilities. *International Journal of Heat and Fluid Flow*, 29:1638–1649, 2008.

[46] P.R. Spalart and S.R. Allmaras. A one-equation turbulence model for aerodynamic flows. *La Recherche Aeŕospatiale*, 1:5–21, 1994.

[47] J. Smagorinsky. General Circulation Experiments with the Primitive Equations I.The basic Experiment. *Monthly Weather Review*, 91:99–164, 1963.

[48] S.-H. Peng. Hybrid RANS-LES Modeling based on Zero- and One-Equation Models for Turbulent Flow Simulation. In *Proceedings of 4th International Symposium on Turbulence and Shear Flow Phenomena*, volume 3, pages 1159–1164, Williamsburg, USA, 27-29 June 2005.

[49] S.-H. Peng. Algebraic Hybrid RANS-LES Modelling Applied to Incompressible and Compressible Turbulent Flows. In *36th Fluid Dynamics Conference and Exhibit*, San Francisco, USA, 5-8 June 2006. AIAA paper 2006-3910.

[50] B.S. Baldwin and H. Lomax. Thin Layer Approximation and Algebraic Model for Separated Turbulent Flows. In *16th Aerospace Sciences Meeting*, Huntsville, USA, 1978. AIAA.

[51] J.C. Kok and H. van der Ven. Capturing free shear layers in hybrid RANS-LES simulations of separated flow. In *Second Symposium "Simulation of Wing and Nacelle Stall"*, Braunschweig, Germany, 21-22 June 2012.

[52] L. Davidson and S.-H. Peng. Embedded LES using PANS. In *6th AIAA Theoretical Fluid Mechanics Conference*, Honolulu, USA, 27-30 June 2011. AIAA paper 2011-3108.

[53] A.G. Kravchenko and P. Moin. On the Effect of Numerical Errors in Large Eddy Simulation of Turbulent Flows. *Journal of Computational Physics*, 131:310–322, 1997.

[54] J.C. Kok. A high-order low-dispersion symmetry-preserving finite-volume method for compressible flow on curvilinear grids. *Journal of Computational Physics*, 228:6811–6832, 2009.

[55] U. Piomelli, W.H. Cabot, P. Moin, and S. Lee. Subgrid-Scale backscatter in turbulent and transitional flows. *Physics of Fluids*, 3:1766–1771, 1991.

[56] D. Carati, S. Ghosal, and P. Moin. On the representation of backscatter in dynamic localization models. *Physics of Fluids*, 7:606–616, 1995.

[57] S.-H. Peng. Hybrid RANS-LES modelling with an energy backscatter function incorporated in the LES mode. In *Turbulence, Heat and Mass Transfer 7*. Begell House, 2012.

[58] S.-H. Peng and L. Davidson. Approximation of subgrid-scale stresses based on the Leonard expansion. In K. Hanjalic, Y. Nagano, and S. Jakirlic, editors, *Turbulence, Heat and Mass Transfer 6*. Begell House, 2009.

[59] L. Davidson. Hybrid LES-RANS: back scatter from a scale-similarity model used as forcing. *Philosophical Transactions of the Royal Society*, 367:2905–2915, 2009.

[60] J.C. Kok and H. van der Ven. Destabilizing Free Shear Layers in X-LES Using a Stochastic Subgrid-Scale Model. In *Progress in Hybrid RANS-LES Modelling*, volume 111, pages 179–189. Springer, 2010.

[61] E. Leveque, F. Toschi, L. Shao, and J.-P. Bertoglio. Shear-improved Smagorinsky model for large-eddy simulation of wall-bounded turbulent flows. *Journal of Fluid Mechanics*, 570:491–502, 2007.

[62] M. Breuer, N. Jovicic, and K. Mazaev. Comparison of DES, RANS and LES for the separated flow around a flat plate at high incidence. *International Journal for Numerical Methods in Fluids*, 41:357–388, 2003.

[63] N. Chauvet, S. Deck, and L. Jacquin. Zonal Detached Eddy Simulation of a Controlled Propulsive Jet. *AIAA Journal*, 45:2458–2473, 2007.

[64] M.J. Lighthill. On Sound Generated Aerodynamically. I. General Theory. *Proceedings of the Royal Society of London. Series A, Mathematical and Physical Sciences*, 211:564–587, 1952.

[65] M.J. Lighthill. On Sound Generated Aerodynamically. II. Turbulence As A Source Of Sound. *Proceedings of the Royal Society of London. Series A, Mathematical and Physical Sciences*, 222:1–32, 1954.

[66] G. Kirchhoff. Zur Theorie der Lichstrahlen. *Annalen der Physik*, 254:663–695, 1883.

[67] A.S. Lyrintzis. Review: The Use of Kirchhoff's Method in Computational Aeroacoustics. *Journal of Fluids Engineering*, 116:665–676, 1994.

[68] K.S. Brentner and F. Farassat. An Analytical Comparison of the Acoustic Analogy and Kirchhoff Formulation for Moving Surfaces. *AIAA Journal*, 336:1379–1386, 1998.

[69] B. Nebenführ, S.-H. Peng, and L. Davidson. Precursor RANS computations for the F15 three-element high-lift configuration. Technical Report FOI Memo 2865, Chalmers/FOI, 2011.

[70] B. Nebenführ, S.-H. Peng, and L. Davidson. Hybrid RANS-LES Simulation of Turbulent High-Lift Flow in Relation to Noise Generation. In S. Fu et al., editor, *Progress in Hybrid RANS-LES Modelling, NNFM*, volume 117. Springer, 2012.

[71] B. Nebenführ, H.-D. Yao, S.-H. Peng, and L. Davidson. Hybrid RANS-LES Simulation for Aerodynamic and Aeroacoustic Analysis of a Multi-Element Airfoil. To be published, 2013.

[72] D.C. Wilcox. Reassessment of the Scale-Determining Equation for Advanced Turbulence Models. *AIAA Journal*, 26:1299–1310, 1988.

[73] D.C. Wilcox. Simulation of Transition with a Two-Equation Turbulence Model. *AIAA Journal*, 32:247–255, 1994.

[74] F.R. Menter. Two-Equation Eddy-Viscosity Turbulence Models for Engineering Applications. *AIAA Journal*, 32:1598–1605, 1994.

[75] S.-H. Peng, L. Davidson, and S. Holmberg. A Modified Low-Reynolds-Number $k-\omega$ Model for Recirculating Flows. *Journal of Fluids Engineering*, 119:867–875, 1997.

[76] Edge User Guide, Issue 5.2.0, 2011.

[77] Edge Theoretical Formulation, Issue 5.2.0, 2011.

[78] M.R. Khorrami. Understanding Slat Noise Sources. In *Computational Aeroacoustics: From Acoustic Sources Modeling to Far-Field Radiated Noise Prediction Colloquium EUROMECH 449*, Chamonix, France, 9-12 December 2003.

[79] L.N. Jenkins, M.R. Khorrami, and M.M. Choudhari. Characterization of Unsteady Flow Structures Near Leading-Edge Slat: Part I. PIV Measurements. In *10th AIAA Aeroacoustics Conference*, Manchester, UK, 10-12 May 2004. AIAA paper 2004-2801.

[80] F. Farassat. Discontinuities in Aerodynamics and Aeroacoustics: The Concept and Applications of Generalized Derivatives. *Journal of Sound and Vibration*, 55(2):165–193, 1977.

Appendix A

Derivation of acoustic analogies

The three acoustic analogies used in this work, are derived similarly to each other. However, the derivation of the Curle and FWH analogies starts from the compressible Navier-Stokes equations, while the Kirchhoff analogy is derived from the homogeneous wave equation. The mathematical tools needed for the derivations are the same in all cases, regardless the starting point. In the following, the derivations of the FWH method for a permeable surface and the Kirchhoff method will be given.

A.1 Generalized functions

A powerful mathematical tool used in the derivation of acoustic analogies is the theory of generalized functions. Generalized function theory is in particular useful for enabling to treat discontinuous functions in the same way as smooth functions. Despite the fact that understanding the field of generalized functions requires considerable mathematical capabilities, it will suffice to understand generalized differentiation for the purpose of following the derivation of acoustic analogies.

We consider a function $h(x)$ that is piecewise smooth with a discontinuity at x_0. The discontinuity at x_0 is expressed as a step $\Delta h = h(x_{0+}) - h(x_{0-})$. Generalized derivatives are denoted by an overbar in the following. For the function $h(x)$, the generalized derivative is given by

$$\frac{\bar{d}h}{dx} = \bar{h}'(x) = h'(x) + \Delta h \delta(x - x_0) \tag{A.1}$$

where $h'(x)$ is the ordinary derivative of $h(x)$, which is not defined at the discontinuity and $\delta(x)$ is the Dirac delta function. It can be seen that the generalized derivative is equal the ordinary derivative, except at the discontinuity, $x = x_0$.

As a next step, $q(\vec{x})$ is considered a function of $\vec{x} = (x_1, x_2, x_3)$ with a discontinuity over a surface $f(\vec{x}) = 0$. Analogically to before, the step across the surface is defined as $\Delta q = q(f = 0_+) - q(f = 0_-)$. Note that $q(f = 0_+)$ is on the outside of the surface $f = 0$. The gradient ∇f points in the outward normal direction. We assume that the discontinuity lies in the direction normal to the surface. It is then possible to introduce a surface coordinate system, $\vec{u} = (u_1, u_2, u_3)$, so that u_1 and u_2 are spanning a plane parallel to the surface and $u_3 = f$ is normal to the surface. The discontinuity is then found only in direction u_3. Hence, the generalized derivatives in u_1 and u_2

direction are identical to the ordinary partial derivatives and in the direction of u_3 the generalized derivative can be written with the help of Eq. (A.1), so that

$$\frac{\bar{\partial} q}{\partial u_i} = \frac{\partial q}{\partial u_i} \qquad \text{for } i = 1, 2 \tag{A.2a}$$

$$\frac{\bar{\partial} q}{\partial u_3} = \frac{\partial q}{\partial u_3} + \Delta q \delta(u_3) \tag{A.2b}$$

In order to find $\bar{\partial} q / \partial x_i$, we multiply Eqs. (A.2a) and (A.2b) with $\partial u_j / \partial x_i$ and obtain

$$\begin{aligned} \frac{\bar{\partial} q}{\partial x_i} &= \frac{\bar{\partial} q}{\partial u_j} \frac{\partial u_j}{\partial x_i} \\ &= \frac{\partial q}{\partial u_j} \frac{\partial u_j}{\partial x_i} + \Delta q \frac{\partial u_3}{\partial x_i} \delta(u_3) \\ &= \frac{\partial q}{\partial x_i} + \Delta q \frac{\partial f}{\partial x_i} \delta(f) \end{aligned} \tag{A.3}$$

where $\partial q / \partial x_i$ is the ordinary partial derivative of the function $q(\vec{x})$. In vector form, Eq. (A.3) can be written as

$$\bar{\nabla} q = \nabla q + \Delta q \nabla f \delta(f) \tag{A.4}$$

A.2 Derivation of the FWH analogy

We define a moving surface $f(\vec{x}, t) = 0$ that is assumed to enclose all the noise sources in a flow. The interior of the surface is $f < 0$ and the region outside the surface is denoted by $f > 0$. Also the surface is assumed to be defined such that $\nabla f = \vec{n}$ is the outward pointing unit normal vector. The surface is considered permeable and the flow variables on the inside of f are assigned their freestream values as illustrated in Fig. A.1.

$$\tilde{\rho} = \begin{cases} \rho & f > 0 \\ \rho_0 & f < 0 \end{cases} \tag{A.5}$$

$$\rho \tilde{u}_i = \begin{cases} \rho u_i & f > 0 \\ 0 & f < 0 \end{cases} \tag{A.6}$$

$$\tilde{P}_{ij} = \begin{cases} P_{ij} & f > 0 \\ 0 & f < 0 \end{cases} \tag{A.7}$$

where $\tilde{\cdot}$ denotes a generalized quantity and subscript 0 denotes the freestream value. The quantities ρ, ρu_i and P_{ij} are the density, momentum and compressive stress tensor as defined by Lighthill [64], respectively. Note, that the viscous stresses in P_{ij} are neglected here and hence $P_{ij} = (p - p_0)\delta_{ij}$. In the region $f > 0$, the flow is governed by the Navier-Stokes equations:

$$\frac{\partial \rho}{\partial t} + \frac{\partial}{\partial x_i}(\rho u_i) = 0 \tag{A.8a}$$

$$\frac{\partial}{\partial t}(\rho u_i) + \frac{\partial}{\partial x_j}(\rho u_i u_j + P_{ij}) = 0 \tag{A.8b}$$

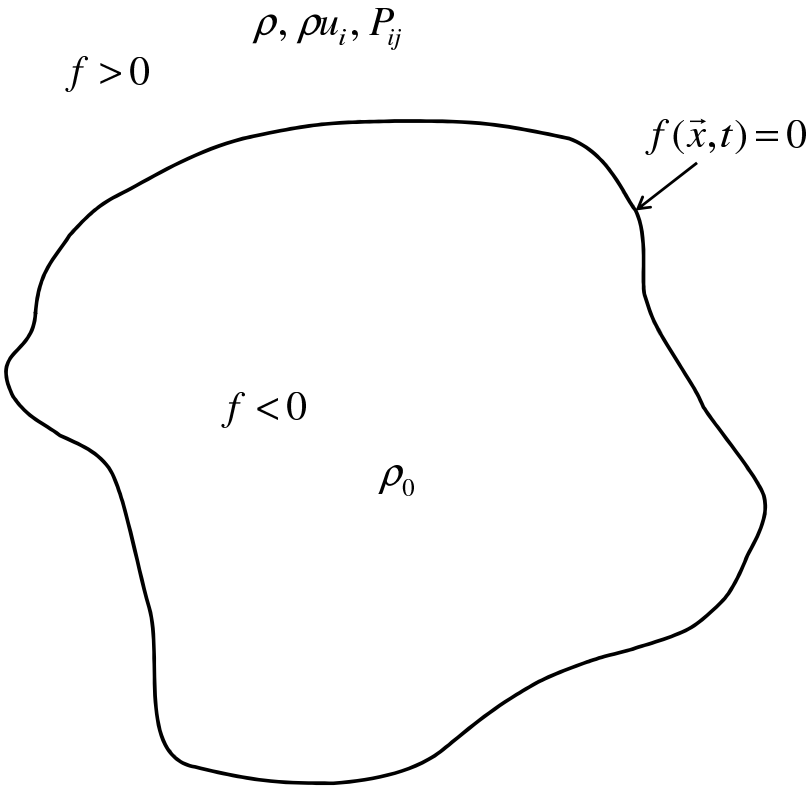

Figure A.1: Schematic drawing of a FWH surface.

Equation (A.8a) is the continuity equation. It is possible, to replace the flow variables with the generalized variables from Eqs. (A.5)–(A.7). Since, this introduces an artificical discontinuity at the surface $f = 0$, generalized derivatives have to be utilized.

$$\begin{aligned}\frac{\bar{\partial}\tilde{\rho}}{\partial t} + \frac{\bar{\partial}}{\partial x_i}(\rho\tilde{u}_i) = \frac{\partial \rho}{\partial t} + (\rho - \rho_0)\frac{\partial f}{\partial t}\delta(f) \\ + \frac{\partial}{\partial x_i}(\rho u_i) + (\rho u_i)\frac{\partial f}{\partial x_i}\delta(f)\end{aligned} \tag{A.9}$$

where $\partial f/\partial t = -v_n$ is the velocity of the moving surface and $\partial f/\partial x_i = n_i$ are the components of the outward pointing unit normal vector. The steps at $f = 0$ are represented by $\Delta\rho = (\rho - \rho_0)$ and $\Delta\rho u_i = (\rho u_i - 0) = \rho u_i$. The right-hand side of Eq. (A.9) can be simplified with the help of Eq. (A.8a), which is represented by the first and the third term. Due to that, the following generalized continuity equation is obtained:

$$\frac{\bar{\partial}\tilde{\rho}}{\partial t} + \frac{\bar{\partial}}{\partial x_i}(\rho\tilde{u}_i) = [\rho_0 v_n + \rho(u_n - v_n)]\delta(f) \tag{A.10}$$

where $u_n = u_i(\partial f/\partial x_i) = u_i n_i$ is the fluid velocity normal to the surface. It can be seen that the artificial discontinuity has produced source terms on the right-hand side of the equation. In an analogical way, the generalized momentum equation

with non-zero source terms can be found.

$$\begin{aligned}\frac{\bar{\partial}}{\partial t}(\rho\tilde{u}_i) + \frac{\bar{\partial}}{\partial x_j}(\rho\tilde{u}_i u_j + \tilde{P_{ij}}) &= \frac{\partial}{\partial t}(\rho u_i) + \rho u_i \frac{\partial f}{\partial t}\delta(f) \\ &+ \frac{\partial}{\partial x_j}(\rho u_i u_j + P_{ij}) + (\rho u_i u_j + \Delta P_{ij})\frac{\partial f}{\partial x_j}\delta(f) \\ &= [\rho u_i(u_n - v_n) + (p - p_0)\delta_{ij}n_j]\delta(f)\end{aligned} \tag{A.11}$$

with $\Delta P_{ij} = (p - p_0)\delta_{ij}$, since the viscous stresses in P_{ij} are neglected. In order to obtain a wave equation, $\bar{\partial}/\partial t$ is taken of both sides of Eq. (A.10) and $\bar{\partial}/\partial x_i$ is taken of both sides of Eq. (A.11). Now, we can subtract the latter from the former, which yields:

$$\begin{aligned}&\frac{\bar{\partial}^2\tilde{\rho}}{\partial t^2} - \frac{\bar{\partial}^2}{\partial x_i x_j}(\rho\tilde{u}_i u_j + \tilde{P_{ij}}) = \\ &= \frac{\bar{\partial}}{\partial t}([\rho_0 v_n + \rho(u_n - v_n)]\delta(f)) - \frac{\bar{\partial}}{\partial x_i}([\rho u_i(u_n - v_n) + (p - p_0)\delta_{ij}n_j]\delta(f))\end{aligned} \tag{A.12}$$

Finally, $\bar{\nabla}^2[c_0^2(\rho - \rho_0)]$ is subtracted from both sides of Eq. (A.12).

$$\begin{aligned}\frac{\bar{\partial}^2\tilde{\rho}}{\partial t^2} - \bar{\nabla}^2[c_0^2(\rho - \rho_0)] - \frac{\bar{\partial}^2}{\partial x_i x_j}(\rho\tilde{u}_i u_j + \tilde{P_{ij}}) &= \\ &= \frac{\bar{\partial}}{\partial t}([\rho_0 v_n + \rho(u_n - v_n)]\delta(f)) \\ &- \frac{\bar{\partial}}{\partial x_i}([\rho u_i(u_n - v_n) + (p - p_0)\delta_{ij}n_j]\delta(f)) \\ &- \bar{\nabla}^2[c_0^2(\rho - \rho_0)]\end{aligned} \tag{A.13}$$

The above equation can be rearranged in the following way:

$$\begin{aligned}\frac{\bar{\partial}^2\tilde{\rho}}{\partial t^2} - \frac{\bar{\partial}^2}{\partial x_i x_i}[c_0^2(\rho - \rho_0)] &= \\ &= \frac{\bar{\partial}}{\partial t}([\rho_0 v_n + \rho(u_n - v_n)]\delta(f)) \\ &- \frac{\bar{\partial}}{\partial x_i}([\rho u_i(u_n - v_n) + (p - p_0)\delta_{ij}n_j]\delta(f)) \\ &+ \frac{\bar{\partial}^2}{\partial x_i x_j}(\rho\tilde{u}_i u_j + \tilde{P_{ij}}) + -\frac{\bar{\partial}^2}{\partial x_i x_i}[c_0^2(\rho - \rho_0)]\end{aligned} \tag{A.14}$$

The wave operator can be introduced on the left-hand side of Eq. (A.14), as a result of the replacements $\rho' = \rho - \rho_0$ and $p' = c_0^2\rho'$. The substitution $p' = c_0^2\rho'$ is justified, since outside the surface linear wave propagation is assumed.

$$\begin{aligned}\bar{\Box}^2 p'(\vec{x}, t) = &- \frac{\bar{\partial}}{\partial x_i}([\rho u_i(u_n - v_n) + (p - p_0)\delta_{ij}n_j]\delta(f)) \\ &+ \frac{\bar{\partial}}{\partial t}([\rho_0 v_n + \rho(u_n - v_n)]\delta(f)) \\ &+ \frac{\bar{\partial}^2}{\partial x_i x_j}[T_{ij}H(f)]\end{aligned} \tag{A.15}$$

where $T_{ij} = [\rho u_i u_j + P_{ij} - c_0^2(\rho - \rho_0)\delta_{ij}]$ is the Lighthill tensor and $H(f)$ is the Heaviside function as to remember that the third term on the right-hand side only exists outside to the surface. As the Lighthill tensor is only defined exterior to the surface, the tilde denoting generalized function has been dropped here. Note that the Curle analogy can be derived from Eq. (A.15) by assuming a stationary and solid surface. In the case of a stationary and solid surface, $u_i = u_j = v_n = 0$ and hence the Curle equation is returned.

$$\begin{aligned}\bar{\Box}^2 p'(\vec{x},t) = &- \frac{\bar{\partial}}{\partial x_i}[p' n_i \delta(f)] \\ &+ \frac{\bar{\partial}^2}{\partial x_i x_j}[T_{ij} H(f)]\end{aligned} \tag{A.16}$$

A.3 Derivation of the Kirchhoff analogy

In the Kirchhoff analogy, a surface $f = 0$ is defined that encloses all aeroacoustic sources so that in the region exterior to the surface, the homogeneous wave equation is fulfilled. Here, we now assume the surface to be permeable and stationary.

$$\frac{1}{c_0^2}\frac{\partial^2 p'}{\partial t^2} - \nabla^2 p' \equiv \Box^2 p'(\vec{x},t) = 0 \tag{A.17}$$

Now, the pressure in Eq. (A.17) is replaced by a discontinuous function, $\tilde{p}'$, such that it exists outside of the surface whereas it is set to zero inside the surface.

$$\tilde{p}' = \begin{cases} p' & f > 0 \\ 0 & f < 0 \end{cases} \tag{A.18}$$

This substitution makes it necessary to use generalized derivatives in Eq. (A.17), since $\Box^2 \tilde{p}'$ is not defined and thus an expression for $\bar{\Box}^2 \tilde{p}'$ has to be found. One can take the generalized derivative of the time-derivative of pressure leading to

$$\frac{\bar{\partial} p'}{\partial t} = \frac{\partial p'}{\partial t} + \Delta p' \frac{\partial f}{\partial t}\delta(f) = \frac{\partial p'}{\partial t} \tag{A.19}$$

Note, that $\partial f/\partial t = 0$ for a stationary surface. By exploitation of Eq. (A.19), the generalized second time-derivative can be written as follows:

$$\frac{\bar{\partial}^2 p'}{\partial t^2} = \frac{\partial^2 p'}{\partial t^2} \tag{A.20}$$

The generalized Laplace operator can be derived with the help of Eq. (A.4) as

$$\begin{aligned}\bar{\nabla}^2 p' &= \bar{\nabla} \cdot (\bar{\nabla} p') = \\ &= \bar{\nabla} \cdot \left[\nabla p' + \Delta p' \frac{\partial f}{\partial x_i}\delta(f)\right] \\ &= \nabla \cdot (\nabla p') + \Delta(\nabla p')\frac{\partial f}{\partial x_i}\delta(f) + \bar{\nabla} \cdot \left[\Delta p' \frac{\partial f}{\partial x_i}\delta(f)\right] \\ &= \nabla^2 p' + \Delta(\nabla p')\frac{\partial f}{\partial x_i}\delta(f) + \bar{\nabla} \cdot \left[\Delta p' \frac{\partial f}{\partial x_i}\delta(f)\right]\end{aligned} \tag{A.21}$$

Utilizing the expressions of Eqs. (A.20) and (A.21) for developing an expression for $\bar{\Box}^2\tilde{p}'$ yields then:

$$\bar{\Box}^2\tilde{p}'(\vec{x},t) = \Box^2\tilde{p}' - \Delta(\nabla p')\frac{\partial f}{\partial x_i}\delta(f) - \bar{\nabla}\cdot\left[\Delta p'\frac{\partial f}{\partial x_i}\delta(f)\right] \tag{A.22}$$

where $\Delta p' = p'$ and $\Delta(\nabla p') = \partial p'/\partial x_i$. The ordinary wave operator $\Box^2\tilde{p}' = 0$ and hence, Eq. (A.22) can be rewritten as:

$$\bar{\Box}^2\tilde{p}'(\vec{x},t) = -\frac{\partial p'}{\partial n}\delta(f) - \frac{\bar{\partial}}{\partial x_i}[p' n_i \delta(f)] \tag{A.23}$$

with $\bar{\partial}p'/\partial n = (\bar{\partial}p'/\partial x_i)n_i$.